

## GLOBAL HYDROMAGNETIC SIMULATIONS OF A PLANET EMBEDDED IN A DEAD ZONE: GAP OPENING, GAS ACCRETION AND FORMATION OF A PROTOPLANETARY JET

O. GRESSEL<sup>1,2</sup>, R. P. NELSON<sup>2</sup>, N. J. TURNER<sup>3</sup>, U. ZIEGLER<sup>4</sup>

<sup>1</sup>NORDITA, KTH Royal Institute of Technology and Stockholm University, Roslagstullsbacken 23, 106 91 Stockholm, Sweden

<sup>2</sup>Astronomy Unit, Queen Mary University of London, Mile End Road, London E1 4NS, UK

<sup>3</sup>Jet Propulsion Laboratory, California Institute of Technology, Pasadena, CA 91109, USA

<sup>4</sup>Leibniz-Institut für Astrophysik Potsdam (AIP), An der Sternwarte 16, 14482, Potsdam, Germany

*Draft version February 13, 2019*

### ABSTRACT

We present the results of 3D global hydrodynamic and magnetohydrodynamic (MHD) simulations of accreting planets embedded in protoplanetary disks (PPDs). The MHD calculation includes an Ohmic resistivity depending on the density, temperature and overlying mass column, leading to a layered disk that has turbulent surface layers and an inert dead zone near the midplane. Mesh refinement was used to resolve the flow within the accreting planet Hill sphere. The main results can be summarized as follows: (i) In agreement with previous studies we find that the accretion flow in the planet Hill sphere is intrinsically three dimensional for both laminar and turbulent models. Net inflow toward the planet is dominated by flows that originate from high latitudes. Midplane regions of the quasi-Keplerian circumplanetary disks (CPDs) that form display outflow away from the planet, with a spatial distribution that varies between the models. (ii) Gap opening ignites the dead zone into a turbulent state due to increased ionization in the low density gas. The accreting planet is then embedded in a turbulent environment, leading to stochastic accretion and a quasi-turbulent flow within the Hill sphere. (iii) Advection of gas and magnetic field into the Hill sphere, where it joins the rotating CPD, generates helical fields that launch magnetocentrifugally driven outflows. During one particular time interval we observe that a highly-collimated, one-sided protoplanetary jet is launched from the circumplanetary disk. (iv) The surface density of the CPD is found to be  $\sim 30 \text{ g cm}^{-2}$ , small enough to allow significant ionization and magnetized turbulence to develop. (v) The accretion rate onto the planet in the MHD simulation reaches a steady value of approximately  $8 \times 10^{-3} M_{\oplus} \text{ yr}^{-1}$ . The accretion rates in the viscous laminar disk runs fall below this value, and continue to decrease throughout the simulations without reaching steady values. This is because accretion in the magnetized PPD arises mainly through the surface layers where the effective viscous stresses are large, and impervious to the tidal torques of the planet. Our simulations suggest that gas accretion onto a forming giant planet within a magnetized PPD with dead zone allows rapid growth from Saturnian to Jovian masses and above. Gap opening leads to a turbulent environment from which the planet accretes, leading to an intrinsically three dimensional and highly time dependent flow within the planet Hill sphere and CPD. As well as being relevant for the theory of giant planet formation, these results have important implications for the formation of regular satellite systems around gas giant planets.

*Subject headings:* magnetohydrodynamics – methods: numerical – planets and satellites: formation – protoplanetary disks

### 1. INTRODUCTION

Gas giant planets are widely believed to form *via* core nucleated accretion, a scenario that begins with the formation of a solid rock and ice core in a protoplanetary disk (PPD) by the agglomeration of smaller bodies (planetesimals), and which concludes with the accretion of a gaseous envelope from the surrounding nebula (Mizuno 1980). Although it has been suggested that giant planets may form through the direct gravitational fragmentation of a massive protoplanetary disk during its early evolution (Boss 1998), circumstantial evidence for core accretion having operated in the Solar System is provided by the inferred existence of significant cores in Saturn, Uranus and Neptune (e.g. Saumon & Guillot 2004). It can further be argued that the substantial numbers of relatively low-mass super-Earth and Neptune-like extrasolar planets being discovered (e.g. Lissauer et al. 2011) indicate that core accretion is a common mode of planetary formation outside of the Solar System.

Detailed one-dimensional models of gas giant planet for-

mation indicate that envelope accretion occurs in two distinct stages: (i) a quasi-static contraction phase during which the envelope mass grows slowly over time scales  $\gtrsim 1 \text{ Myr}$  (Pollack et al. 1996); (ii) a runaway growth phase during which the envelope accretes dynamically onto the planet. This later phase normally arises once the envelope exceeds the core mass, corresponding to a total planet mass  $\gtrsim 35 M_{\oplus}$ . Prior to runaway gas accretion the protoplanet remains embedded in the nebula and the bloated envelope is envisaged to connect smoothly onto the surrounding disk. During the runaway phase, however, the planet contracts down to a size  $\simeq 3$  Jupiter radii and gas accretion is expected to occur through a circumplanetary disk (CPD) that forms by the flow of gas into the planet Hill sphere (Papaloizou & Nelson 2005). We note that the 1D envelope calculations indicate that planets with Saturn-like masses ( $\sim 0.2 - 0.6 M_J$ ) are likely to experience maximal gas accretion (Pollack et al. 1996), as the flow onto the planet is relatively unimpeded by the compressional heating of the envelope for these masses. Although these 1D quasi-static calculations cannot determine the details of the hydrodynamic flow, so some doubt remains about

the actual accretion rate, it is noteworthy that extrasolar planets with masses similar to Saturn are common<sup>1</sup> even though existing calculations suggest that once a planet enters the runaway gas accretion phase it should grow rapidly beyond this mass if in the presence of a significant gas reservoir. One motivation for performing the calculations presented in this paper is to address this issue, and examine whether or not a possible bottle-neck exists that can prevent rapid growth of planets in this mass range.

The formation of a gas giant planet through gas accretion and the action of tidal torques leads to the formation of an annular gap around the vicinity of the planet (Lin & Papaloizou 1986; Bryden et al. 1999; Kley 1999; Lubow et al. 1999). This may also herald the transition of the planet’s migration from type I (Ward 1997) during the embedded phase to type II when a gap has formed (Lin & Papaloizou 1986; Nelson et al. 2000). Material then feeds onto the planet through the gap at the viscous supply rate. A detailed understanding of this accretion process necessitates a sophisticated model of the PPD environment in which the planet is embedded.

Global, multidimensional studies of gas accretion onto embedded planets began with 2D flat viscous locally isothermal disk models (Bryden et al. 1999; Kley 1999; Lubow et al. 1999) and suggested that accretion rates onto Jovian mass planets should be  $\sim 10^{-5} M_J \text{ yr}^{-1}$  for disk models with masses close to the minimum mass solar nebula (Hayashi 1981) and canonical values for the disk aspect ratio ( $H/r \sim 0.05$ ) and viscous stress parameter ( $\alpha \sim 10^{-3}$ ). Models that adopt more realistic equations of state and/or are 3D find similar accretion rates (D’Angelo et al. 2003; Klahr & Kley 2006; Paardekooper & Mellema 2008; Ayliffe & Bate 2009b). Typically these simulations do not resolve the flow in the planet Hill sphere very accurately, so although they indicate the presence of a CPD, the simulations are unable to resolve the details of its flow. An exception to this are the calculations by Ayliffe & Bate (2009b), which attempt to simulate the full 3D radiation-hydrodynamic evolution of the planetary envelope and CPD, but unfortunately these are hampered by time step restrictions that prevent long term runs being performed.

Recent 3D hydrodynamic studies of the accretion flow onto giant planets have been performed that focus on the local evolution in the vicinity of the Hill sphere (Machida et al. 2008; Tanigawa et al. 2012). These highly resolved studies have uncovered a particularly interesting result, namely that accretion onto the planet occurs not through the midplane region of the CPD – where the gas flow appears to be *away* from the planet on average – but instead through gas flows that occur at higher latitudes within the planet Hill sphere. The midplane region of the CPD does not appear to act as a traditional accretion disk, but instead is a region where material which enters the Hill sphere with excess angular momentum is spun-out away from the planet. The most recent study of Tanigawa et al. (2012) resolves the flow down to approximately 3% of the Hill sphere radius, and midplane outflow appears to occur all the way down to this region. It is unclear how these results will change when angular momentum transport processes are included in the evolution of the CPD.

All of the above multidimensional studies have either ignored the disk viscosity, or have solved the Navier-Stokes equations by adopting an anomalous value to account for the angular momentum transport arising from turbulence in the

disk, which is believed to be driven by the magnetorotational instability (MRI, Balbus & Hawley 1998). Highly resolved studies of gas accretion onto giant planets embedded in disks that support MRI-turbulence have not been performed, although low resolution studies of gap formation and/or gas accretion have been presented by Nelson & Papaloizou (2003), Winters, Balbus, & Hawley (2003), Papaloizou et al. (2004), and Uribe et al. (2011) for disks that support fully developed turbulence. It was observed that magnetic braking caused an apparent increase in gas accretion in some these simulations, by removal of angular momentum of material entering the Hill sphere, but the low resolution and assumption of ideal magnetohydrodynamics render this observation questionable in terms of its application to real systems. Although these simulations in some ways represent a step-up in realism relative to laminar viscous disk models, the cold dense midplane regions of protoplanetary disks are believed to host dead zones where the magnetic field and gas decouple due to the low ionization levels there, with accretion occurring in the surface layers that are ionized by external sources such as cosmic rays and stellar X-rays (Gammie 1996; Igea & Glassgold 1999).

In this paper, we present the first global simulation of a giant planet embedded in a magnetized protoplanetary disk with a midplane dead zone and actively accreting surface layers, where the larger scale flow features in the planet Hill sphere are resolved. We adopt a resistivity prescription in which the ionization structure changes over time in response to the changing density, temperature and column of material absorbing the X-rays (Gressel et al. 2011, 2012), and examine gap formation and accretion onto the protoplanet. We utilize adaptive mesh refinement to provide good resolution within the planet Hill sphere, resolving the flow with reasonable accuracy down to a distance from the planet equal to 5% of the Hill sphere radius. Similarly resolved hydrodynamic simulations are also presented for comparison purposes. The primary aim is to examine the structure of the gap that forms as the planet accretes gas and exerts tidal torques on the surrounding protoplanetary disk (including the influence of the varying ionization fraction as the gap opens), to examine the flow in the Hill sphere and the rate of gas accretion onto the planet. We find accretion rates that are consistent with the previous studies described above, implying that runaway gas accretion should form planets with Jovian masses and above efficiently if planet formation occurs in a disk with mass similar to the minimum mass nebula. Enlivening of the gap region into a turbulent state leads to a highly time-dependent 3D flow within the gap and planet Hill sphere, with interesting consequences for the dynamics of the circumplanetary disk.

This paper is organized as follows: In Section 2 we formulate the equations and lay out the numerical methods used. The utilized disk model is described in Section 3, where we give initial and boundary conditions and recapitulate our ionization model. General results concerning the PPD are presented in Section 4, followed by Section 5 on the opening of the gap, and Section 6 on the circumplanetary disk. Results on the accretion flow onto the planet are found in Section 7. We finally summarize our findings in Section 8, where we discuss potential implications of our results.

## 2. NUMERICAL METHODS

We perform hydrodynamic (HD) and magnetohydrodynamic (MHD) simulations of protoplanetary accretion disks employing a spherical-polar mesh with adaptive grid refinement around an embedded planetary core. The planet is mod-

<sup>1</sup> Out of 720 confirmed extrasolar planets listed on [exoplanets.org](http://exoplanets.org), approximately 170 have masses in the range  $0.2 - 1 M_J$

eled *via* the gravitational potential of a softened point mass, and its position is kept fixed throughout each simulation. The planet’s mass is allowed to grow during the simulation by accretion of gas from the disk, as detailed below.

### 2.1. Numerical scheme

The simulations presented in this paper were performed using the single-fluid MHD code NIRVANA-III, which is based on a second-order finite volume Godunov scheme (Ziegler 2004) and employs the constrained transport (CT) discretization for an intrinsically divergence-free evolution of the magnetic induction. The code has recently been extended to orthogonal curvilinear meshes (Ziegler 2011), and here we use spherical-polar coordinates  $(r, \theta, \phi)$ , denoting spherical radius, co-latitude and azimuth, respectively. Deviating from the publicly available version of the code, we here use the upwind reconstruction technique of Gardiner & Stone (2008) to obtain the edge-centered electromotive force (EMF) needed within the CT update. We have furthermore generalized the EMF interpolation to curvilinear coordinates (cf. Skinner & Ostriker 2010, for the cylindrical case). The upwind reconstruction avoids stability issues present in the original EMF interpolation scheme by Balsara & Spicer (1999), and the relevance of this to the development of the magneto-rotational instability (MRI) was demonstrated by Flock et al. (2010). By default, NIRVANA-III addresses this issue by implementing the two-dimensional Riemann solver of Londrillo & del Zanna (2004), but we here instead chose the approach taken by Gardiner & Stone, as this allows us to easily use the more accurate HLLD approximate Riemann solver of Miyoshi & Kusano (2005), which provides better numerical accuracy for low-Mach number flows. The benefits of using HLLD when modeling MRI turbulence have been demonstrated by Balsara & Meyer (2010).

### 2.2. Equations solved

For our hydrodynamic calculations, we solve the compressible Navier-Stokes equations subject to a prescribed *enhanced* viscosity, which we estimate from the turbulent stresses occurring in the MRI simulation. The hydromagnetic run employs the standard resistive MHD equations with a position-dependent *molecular* diffusivity  $\eta(\mathbf{r}, t)$ , which we derive self-consistently from a detailed ionization model (see Section 3.3) accounting for irradiation of the disk surface by ionizing sources. The full set of equations in a coordinate system co-rotating with the planet reads<sup>2</sup>

$$\begin{aligned} \partial_t \rho + \nabla \cdot (\rho \mathbf{v}) &= 0, \\ \partial_t (\rho \mathbf{v}) + \nabla \cdot [\rho \mathbf{v} \mathbf{v} + p^* \mathbf{I} - \mathbf{B} \mathbf{B}] &= -\rho \nabla \Phi + \rho \mathbf{a}_i + \nabla \cdot \boldsymbol{\tau}, \\ \partial_t e + \nabla \cdot [(e + p^*) \mathbf{v} - (\mathbf{v} \cdot \mathbf{B}) \mathbf{B}] &= -\rho (\nabla \Phi) \cdot \mathbf{v} + \rho \mathbf{a}_i \cdot \mathbf{v} \\ &\quad + \nabla \cdot [\boldsymbol{\tau} \mathbf{v} + \eta \mathbf{B} \times \mathbf{J}] + \Gamma, \\ \partial_t \mathbf{B} - \nabla \times (\mathbf{v} \times \mathbf{B} - \eta \mathbf{J}) &= 0, \\ \nabla \cdot \mathbf{B} &= 0, \end{aligned} \quad (1)$$

with conserved variables  $\rho$ ,  $\rho \mathbf{v}$ , and the *total* energy  $e = \epsilon + \frac{1}{2} \rho \mathbf{v}^2 + \frac{1}{2} \mathbf{B}^2$ , and where  $\epsilon$  denotes the thermal energy density. We use  $\mathbf{J} = \text{curl}(\mathbf{B})$ , and introduce the total pressure  $p^* = p + \frac{1}{2} \mathbf{B}^2$ . The inertial acceleration due to Coriolis and centrifugal effects is  $\mathbf{a}_i = -2\boldsymbol{\Omega} \times \mathbf{v} - \boldsymbol{\Omega} \times (\boldsymbol{\Omega} \times \mathbf{r})$ ,

<sup>2</sup> Note that for clarity, we have suppressed factors of the permeability  $\mu$  appearing in the equations.

where  $\boldsymbol{\Omega} = \Omega_0 \hat{\mathbf{z}}$  is the axial vector representing the angular frequency at the planet radius, and  $\hat{\mathbf{z}}$  is the unit vector pointing along the rotation axis of the protoplanetary disk. The gravitational potential is composed of the central potential of a solar-mass star (i.e.  $M_\star = M_\odot$ ), and the softened point-mass potential of the planet with mass  $M_p = M_p(t)$ , at the fixed position  $\mathbf{r}_p$ , i.e.,

$$\Phi(\mathbf{r}, t) = -\frac{GM_\star}{|\mathbf{r}|} - \frac{GM_p}{|\mathbf{r} - \mathbf{r}_p|} + \frac{\mathbf{r} \cdot \mathbf{r}_p GM_p}{r_p^3}. \quad (2)$$

The third term appearing in the potential is often referred to as the ‘indirect term’, and it accounts for the fact that our coordinate system has its origin at the position of the star, rather than at the center of mass of the combined system. Note that the gravity of the disk does not act on any of the bodies, and hence it does not appear in the potential function. Even with refined meshes we do not yet resolve the physical radius of the accretion envelope of the planet core. To avoid the singularity of the assumed point-mass potential, the second term in Equation (2) is softened with a smoothing length that is fixed at 5% of the Hill radius corresponding to the initial planet mass of  $100M_\oplus$ . This corresponds to half a grid spacing on the coarse mesh.

For the cases where we evolve an energy equation, we assume a relation,  $p = (\gamma - 1)\epsilon$ , with  $\gamma = 7/5$ . The additional heating and cooling term,  $\Gamma$ , serves the purpose of relaxing the thermal energy  $\epsilon$  towards the initial radial temperature profile  $T_i(R)$  on a local dynamical time scale. The update is implemented operator-split and applies Newtonian cooling according to the equation

$$\frac{1}{\rho} \frac{d\epsilon}{dt} = -\frac{\Omega_K(R)}{2\pi} \left( \frac{\epsilon}{\rho} - \Theta_i(R) \right), \quad (3)$$

where  $\Omega_K(R)$  is the Keplerian rotation frequency as a function of cylindrical radius,  $R$ , and the ideal gas relation is used to compute  $\Theta_i(R) \equiv T_i(R) k_B / (\bar{\mu} m_u (\gamma - 1))$ . While such a treatment is a far cry from a realistic approximation of radiative effects occurring in a real protoplanetary disk, it adds realism over a purely isothermal approach. On a practical level, it successfully suppresses the occurrence of the vertical-shear instability (Nelson et al. 2012) which leads to severe disturbance of the dead-zone layer *via* the excitation of corrugation waves. Such disturbances were encountered in inviscid simulations of a locally isothermal disk with imposed radial temperature profile, but in the locally isothermal run that we present here the inclusion of viscosity in the model also suppresses the vertical shear instability.

The viscous stress tensor,  $\boldsymbol{\tau}$ , appearing in the momentum equation is given by  $\boldsymbol{\tau} = \nu (\nabla \mathbf{v} + (\nabla \mathbf{v})^\top - \frac{2}{3} (\nabla \cdot \mathbf{v}))$ , with  $\nu$  the dynamic viscosity parameter. Ohmic dissipation enters the induction equation *via* the  $\nabla \times (\eta \mathbf{J})$  term. In our explicit time integration scheme, the numerically allowed time step related to dissipative terms scales with the square of the grid spacing. This quickly becomes restrictive when applying mesh refinement, especially in the presence of high values of the viscosity coefficient  $\nu$ , and the diffusivity  $\eta$ . To circumvent these potentially very restrictive time-step constraints, we have adopted the super-time-stepping (STS) scheme, introduced by Alexiades, Amiez, & Gremaud (1996). This concept is based on the idea of applying a sequence of (first-order accurate) forward-Euler sub-steps for the dissipation terms. With an appropriate choice of non-equidistant sub-intervals in time, the scheme gains an advantage over classical

sub-stepping techniques. We here chose the STS parameter  $\nu_{\text{STS}} = 0.02$ , and limit the maximum ratio between the permissive Courant time-step and the STS time-step to 20. We remark that the energy equation contains a divergence of a dissipative flux,  $\tau\mathbf{v} + \eta\mathbf{B} \times \mathbf{J}$ . Comparing to test solutions obtained with the unmodified NIRVANA-III, we have not found any indications that the combination of STS with an associated forward-Euler update of the energy equation leads to spurious results. We remark that a future implementation of the NIRVANA-III code will make use of the more accurate second-order scheme recently proposed by Meyer et al. (2012).

### 3. MODEL DESCRIPTION

Our underlying protostellar disk model aims to resemble the intermediate regions of the early protosolar nebula where giant planet formation is believed to have taken place. The adopted computational domain spans a radial extent of  $r \in [1, 8]$  au. Owing to limited computational resources, we restrict the azimuthal domain to a quarter wedge, i.e.,  $\phi \in [0, \pi/2]$ . The latitudinal grid spans a region  $\theta \in [\pi/2 - \vartheta, \pi/2 + \vartheta]$ , with  $\vartheta = 4.5 H/r$ , i.e., covering four and a half pressure scale heights,  $H$ , on each side of the disk midplane. Unless otherwise indicated, the base grid resolution is chosen as  $N_r \times N_\theta \times N_\phi = 384 \times 96 \times 128$  grid points corresponding to 10.7 grid points per  $H$  in the vertical direction. This coincides with the requirement to reasonably resolve unstable MRI modes. Block-adaptive grid refinement (with blocks of size  $4 \times 4 \times 4$ ) is enabled once the planet potential is switched on. Refined meshes of level  $l = 1, 2, \dots$  have grid spacings of  $2^{-l}$  times the base-level resolution. For reasons of simplicity, the adaptivity is controlled by a purely geometrical criterion. Approximately-spherical regions with  $r_s = 1, 2, 4 r_{\text{H}}$  around the planet are refined with  $l = 3, 2, 1$  levels, respectively. This implies that the Hill sphere ( $r_s = r_{\text{H}}$ ) is always refined at the highest level of  $l_{\text{max}} = 3$ , resulting in a grid resolution of roughly 5 Jovian radii,  $R_{\text{J}}$  in the  $r$ , and  $\theta$  directions, and about 11  $R_{\text{J}}$  in the  $\phi$  direction. Considering the number of grid cells covering the CPD, we note that a planet of mass  $M_{\text{p}} = 150 M_{\oplus}$  located at  $r_{\text{p}} = 3.5$  au will be surrounded by a CPD with radius approximately equal to 40% of the Hill radius, giving  $r_{\text{CPD}} \sim 0.074$  au. The grid-spacings on the most refined level are  $(\Delta_r, \Delta_\theta, \Delta_\phi) = (2.28, 2.05, 5.37) \times 10^{-3}$  au. In the horizontal plane  $r_{\text{CPD}}$  is resolved by approximately 33 cells of length  $\Delta_r$  and 14 cells of length  $\Delta_\phi$ . Assuming a constant aspect ratio of,  $H/r \sim 0.5$ , of the CPD, the scale height of the CPD is resolved by approximately 18 cells at its outer rim. Towards the center the resolution per scale height drops linearly. This suggests that the vertical structure of the CPD should be decently resolved, as should the circulating flow in the horizontal plane. Although magnetic stresses related to larger scale magnetic features in the CPD will be resolved, we note that development of the MRI on small scales in the CPD cannot be followed in our simulations.

It is well known that the spherical-polar mesh is ideally suited to numerically preserve angular momentum within the protoplanetary disk. However, in the vicinity of the planet the grid is essentially Cartesian – in consequence, the angular momentum of the circumplanetary disk is likely less-well conserved. The associated numerical truncation error will contribute to the measured accretion rate onto the planet.

#### 3.1. Equilibrium disk model

We now describe the initial disk model, which is chosen to facilitate comparison of our results with the existing literature.

Although modeling and observations point to the fact that protoplanetary disks are moderately flaring (Watson et al. 2007; Pinte et al. 2008), this results in thin disks at small radii, and is suboptimal for simulating using a spherical-polar grid. A convenient setting is obtained when one prescribes a locally-isothermal temperature,  $T$ , falling-off with inverse cylindrical radius, i.e.,  $T(R) = T_0 (R/R_0)^{-1}$ . It can easily be shown that such a dependence leads to a constant opening ratio  $H/R$  throughout the disk, promoting the use of a spherical-polar domain. If we further prescribe a power-law dependence for the disk midplane density,  $\rho_{\text{mid}}(R) = \rho_0 (R/R_0)^{-3/2}$  and assume independent hydrostatic balance in the vertical and radial direction, respectively, we can solve for an equilibrium initial solution given by:

$$\rho(\mathbf{r}) = \rho_0 \left( \frac{R}{R_0} \right)^{-3/2} \exp \left( \frac{GM_\star}{c_s^2} \left[ \frac{1}{r} - \frac{1}{R} \right] \right), \quad (4)$$

$$\Omega(\mathbf{r}) = \Omega_{\text{K}}(R) \sqrt{\frac{R}{r} - \frac{5}{2} \left( \frac{H}{R} \right)^2}, \quad (5)$$

where we have introduced the isothermal sound speed  $c_s$ , which can be derived as  $c_s^2 = c_{s0}^2 (R/R_0)^{-1}$ . We fix the free parameter  $c_{s0}$  according to a value of  $h \equiv H/R = 0.05$ , noting that  $H \equiv c_s \Omega_{\text{K}}$  where the Keplerian angular velocity  $\Omega_{\text{K}}(R) = \sqrt{GM_\star} R^{-3/2}$ . Note that, via  $r$ , the equilibrium rotation profile has a weak vertical shear. One can also see that in the midplane (i.e. for  $r = R$ ), the flow is sub-Keplerian to order  $(H/R)^2$ , which is a consequence of radial pressure support. We chose the normalization  $\rho_0$  to yield a vertically integrated column density of  $\Sigma = 150 \text{ g cm}^{-2}$  at the location  $R = 5$  au, yielding a total disk mass of  $M_{\text{disk}} \simeq 3.6 M_{\text{J}}$ , i.e., when accounting for the full azimuthal extent of  $2\pi$ . In terms of the disk temperature, we obtain  $T = 540$  K at  $R = 1$  au, and  $T = 108$  K at a distance of 5 au, comfortably outside of the ice-line where water ice condenses. The disk is initially threaded by a weak uniform vertical magnetic field of  $B_z = 3.6$  mG. This corresponds to a midplane  $\beta_{\text{p}} \equiv 2p/B^2$  of  $\sim 3 \times 10^5$  at the location of the planet.

#### 3.2. Boundary conditions

To facilitate the long-term evolution of our disk model, we have to make modifications to the standard boundary conditions (BCs) implemented in NIRVANA-III. With the exception of the azimuthal direction, where we simply apply periodicity, all BCs are based on the ‘‘outflow’’ type, i.e., allowing material to leave the domain, but preventing inflow. To improve robustness at the inner corners of the  $(r, \theta)$  domain, we impose reflecting boundaries in the  $r$  direction beyond  $4H$  in  $\theta$ , and moreover impose Keplerian rotation for  $v_\phi$ .

The boundary conditions applied at the upper and lower disk surfaces for the magnetic field are of the ‘‘perfect conductor’’ type, i.e., enforcing the normal component to be zero at the boundary, and applying zero-gradient extrapolation to the parallel field components. In addition, the BCs have been modified to preserve the constant vertical field, imposed initially. Because of the vertical stratification, the hydrodynamic  $\theta$  boundaries require special attention. It is well known that unsplit finite volume schemes make it hard to exactly preserve a given static equilibrium (see e.g. Zingale et al. 2002). This becomes pronounced at the boundaries because using constant extrapolation of the thermal energy density underestimates the pressure gradient. Not balancing gravity exactly

will induce a standing accretion shock in the first grid cell of the active domain. To obtain a better estimate for the vertical continuation of the disk profiles outside the active domain, we employ a second-order Runge-Kutta shooting method to integrate the equations of hydrostatic equilibrium; thereby reducing the amplitude of spurious boundary effects significantly.

A similar, but somewhat less dramatic, effect is present in the radial direction. Taking into account the additional centrifugal force, we extrapolate the radial equilibrium condition to obtain improved boundary values; aiding the long-term stability of the disk evolution. Furthermore, to avoid reflection of spiral density waves, we have implemented ‘buffer zones’ as described in detail in de Val-Borro et al. (2006). This implies that, in narrow annuli adjacent to the radial domain boundary, we force the density  $\rho$ , energy density  $\epsilon$ , and the velocity  $\mathbf{v}$  back to their initial values. The timescale of this process is proportional to the local dynamical time scale, and is smoothly tapered-off with increasing separation from the inner and outer radial boundaries.

### 3.3. The ionization model

The central aim of this work is to develop realistic MHD models for protoplanetary accretion disks containing gaps opened by embedded planets. This requires that we obtain a self-consistent distribution of the disk’s ionization fraction. For our new global models, we largely follow the approach taken in the local box models described in detail in Gressel et al. (2011, 2012) – with the exception that the dependence on the radial coordinate is now included explicitly, rather than being evaluated at the reference radius of the box model.

The disk’s ionization balance is heavily affected by the presence of small dust grains (Sano et al. 2000; Ilgner & Nelson 2006). The associated short adsorption time scale of free electrons makes it prohibitive to follow the detailed non-equilibrium chemistry. Instead, we adopt a simplified approach employing a precomputed table based on the reaction network used for `model4` of Ilgner & Nelson (2006). As before, we consider the contributions of all the charged species following equations (21)-(31) in Wardle (2007). When deriving the resistivity  $\eta(\mathbf{r}, t)$ , we restrict ourselves to the case of Ohmic resistivity, which is a reasonable assumption for the denser parts of the PPD (see, e.g. Wardle 2007) under weak magnetic fields. Our choice is mainly motivated by reasons of tractability as the effect of ambipolar diffusion (and Hall EMFs) will greatly increase the computational complexity of the model. Recent work points to the potential importance of including these additional non-ideal MHD effects (Wardle & Salmeron 2012; Bai & Stone 2013), and our longer term intention is to explore these on a case-by-case basis rather than presenting a “kitchen-sink” simulation from the outset.

For reference, we briefly recapitulate the parameters entering our model (cf. Gressel et al. 2011). We presume dust with density  $\rho_s = 3 \text{ g cm}^{-3}$  and of a single grain size  $d = 0.1 \mu\text{m}$ , which is further assumed to be depleted (by grain growth) to yield a dust-to-gas mass ratio of  $10^{-3}$ . Reactions involving gas-phase ions are represented by Magnesium, which is partly bound-up in grains and hence taken to be depleted by  $10^4$  compared to its solar abundance. In the reaction network, free electrons are created according to the ionization rate  $\zeta(\mathbf{x}, t)$ , which we evaluate based on the external irradiation. The ionization fluxes are attenuated by the integrated columns of gas to the upper and lower disk surfaces, respectively. The den-

sity integration is complicated by the requirement to match the integrals at mesh refinement boundaries, which demands expensive communications. To reduce computational overheads, we store  $\eta(\mathbf{r}, t)$  as a passive scalar variable. This allows us to only update  $\eta$  from integrated densities every three computational time-steps, which is short enough to reflect potential changes of  $\eta$  on dynamical time scales.

The underlying ionization prescription used here comprises stellar X-rays, radionuclides, and energetic protons, and is based on the work of Turner & Drake (2009). We closely follow their approach, and restrict ourselves to stellar X-rays (XRs), and interstellar cosmic rays (CRs) as the prime ionizing agents. The attenuation of interstellar CRs within a PPD has been studied by Umebayashi & Nakano (2009), who derived a dependence

$$\zeta_{\text{CR}} = 5 \times 10^{-18} \text{ s}^{-1} e^{-\Sigma_a/\Sigma_{\text{CR}}} \left[ 1 + \left( \frac{\Sigma_a}{\Sigma_{\text{CR}}} \right)^{\frac{3}{4}} \right]^{-\frac{4}{3}}, \quad (6)$$

with  $\Sigma_{\text{CR}} = 96 \text{ g cm}^{-2}$  a typical cosmic ray attenuation depth (cf. Umebayashi & Nakano 1981), and with an according contribution from the second gas column  $\Sigma_b$ . As in previous work, we use a simple fit to the Monte-Carlo radiative transfer calculations of Igea & Glassgold (1999), and approximate the XR ionization rate via

$$\zeta_{\text{XR}} = 2.6 \times 10^{-15} \text{ s}^{-1} \left[ e^{-\Sigma_a/\Sigma_X} + e^{-\Sigma_b/\Sigma_X} \right] r_{\text{au}}^{-2}, \quad (7)$$

with  $\Sigma_a$  and  $\Sigma_b$  being the column densities to the upper and lower disk surface, respectively, and where  $\Sigma_X = 8.0 \text{ g cm}^{-2}$  is a characteristic absorption depth. We finally include an ambient ionization due to the decay of short-lived radionuclides (SR). As in previous models (Gressel et al. 2012), the related ionization rate is enhanced  $10\times$  compared to the nominal value of  $\zeta_{\text{SR}} = 3.7 \times 10^{-19} \text{ s}^{-1}$  (see Turner & Drake 2009). This is done to provide a ceiling on the resistivity so that the associated time step size does not become prohibitively small. In conclusion, we remark that when a gap is formed in the disk, ideally one should include the radial illumination of the gap edges by the star. For reasons of simplicity, however, we neglect this effect in our current models.

### 3.4. The accretion sink

Even with the aid of adaptive mesh refinement, it remains prohibitive to resolve the gaseous envelope accreting onto the planetary core. This is to say that fidelity of resolving small spatial scales is traded-off against the ability to cover the (comparatively long) time scale on which gap formation occurs. At the same time, making meaningful predictions about the envelope of hot accreting gas will require proper treatment of radiative effects, which are not currently addressed by our model. Instead focusing on the impact of magnetic fields, we are hence interested in asking the question whether the exterior of the accretion region (i.e. the system comprised of the PPD gap, spiral arms and the CPD) can, in fact, provide the material into the sphere of influence of the core.

Our accretion sink is similar to that used in Kley (1999) in that a fixed fraction of material is removed from the direct vicinity of the planet each time step. Unlike in earlier work, we specify the time scale for removal as the local free-fall time (of a test-particle)

$$\tau_{\text{ff}} = \frac{\pi}{2} \sqrt{\frac{r_{\text{acc}}^3}{2GM_p}}, \quad (8)$$

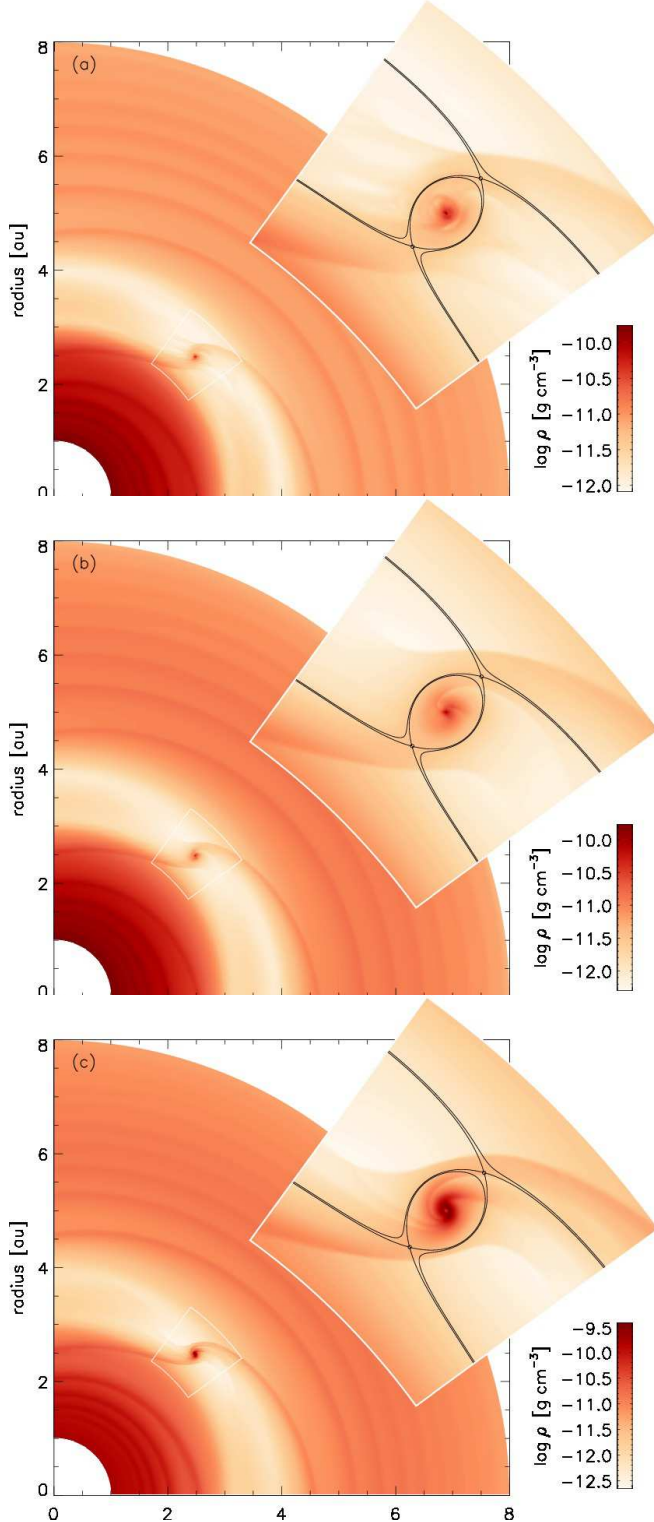


FIG. 1.— Midplane slices of  $\log(\rho)$ . From top to bottom: (a) MHD run, (b) HD run with cooling, (c) isothermal HD run. Black contours indicate the potential surfaces passing through the Lagrange points L1 and L2.

where  $r_{\text{acc}}$  is defined as 5% of the planet’s Hill radius – corresponding roughly to Callisto’s semi-major axis. This amounts to a small fraction of the mass within a sphere of  $r_{\text{acc}}$  being removed per time step. To avoid discontinuous behavior in the accretion flow near the planet, removal is weighted with a three-dimensional Gaussian kernel. Owing to limited com-

putational resources, the mass augmented to the planet is artificially enhanced fourfold to facilitate a speed-up of the gap formation process. In cases where we evolve an energy equation, the modification to the gas density is accompanied by a correction in the thermal energy density as to keep the temperature constant. Within a sphere of  $2r_{\text{acc}}$ , we apply additional cooling to avoid the buildup of strong pressure gradients that would otherwise modify the accretion flow unphysically and retard the flow of gas toward the sink hole. In this region, the temperature is relaxed towards the initial model on a time scale proportional to the Keplerian angular velocity with respect to the planet potential, resulting in temperatures similar to those observed in the radiation-hydrodynamic simulations of Klahr & Kley (2006). To conclude this section, we note that we do not expect a strong numerical effect from the particular scheme adopted for the accretion sink (cf. figure 3 in Machida et al. 2008).

#### 4. PROTOPLANETARY DISK

Previous studies using both laminar and magnetized-turbulent disks have shown that the presence of an accreting gas giant planet leads to gap formation, and the formation of a circumplanetary disk surrounding the planet.

The main goals of this paper are to study the effects of magnetic fields and time-dependent ionization levels on the evolution of the gap, the circumplanetary disk, and the gas accretion rate onto the planet. To achieve these goals it is necessary to develop a fiducial hydrodynamic model for comparison purposes. Coming up with a realistic proxy for a layered turbulent accretion disk is a formidable task in its own right. Clearly, in the presence of a dead-zone, a height-dependent  $\alpha$  should be used (e.g. Pierens & Nelson 2010). Ideally, one would obtain an estimate of the dead-zone structure based on empirical fits derived from MHD simulations (Okuzumi & Hirose 2011), but a simple prescription with  $z/H$  is rendered problematic with the presence of a gap because  $\alpha$  then varies spatially and temporally. For lack of better alternatives, we resort to a standard Shakura-Sunyaev  $\alpha$  viscosity with a constant  $\alpha_{\text{SS}} = 3.25 \times 10^{-3}$ . This value is derived from globally averaged turbulent stresses (normalized with the vertically-averaged gas pressure) in the MHD model, after a quasi-steady state is reached and before the planet is inserted (also cf. Uribe et al. 2011, who use a value of  $2 \times 10^{-3}$ ). In comparison to our fiducial box model (Gressel et al. 2011), which was located at 5 au, we obtain local values (normalized with the midplane gas pressure) of  $\alpha \simeq 3 \times 10^{-3}$  in the active layer, which is dominated by Maxwell stresses, and  $\alpha \simeq 3 \times 10^{-4}$  in the dead-zone layer due to residual Reynolds stresses. We note that the level of turbulence is about a factor of five lower than in the box simulation, which we attribute to the three-fold weaker net-vertical field of  $B_z = 3.6$  mG. For the particular problem of a giant planet embedded in a disk the approach used in the viscous non-magnetized disks probably yields reasonable results because the main driver of evolution on large scales is global angular momentum transport (Nelson & Papaloizou 2003). This argument is supported by our results which show similar planetary accretion rates for the magnetized and non-magnetized disk models described later in this paper.

##### 4.1. Simulation runs

We focus on three simulations in this paper, which are based on the disk model described in Section 3, and all employ three levels of mesh refinement. Each of the simulations is evolved

for roughly 100 planet orbits after the planet is inserted. At the heart of our study is a full-blown, MHD model based on a *physical* resistivity. Within this run, due to the shielding of external ionization, a realistic dead-zone emerges along with self-consistent MRI-active disk surface layers. Moreover, this MHD model, that we refer to as “M1”, is non-isothermal in that an energy equation is solved based on an adiabatic equation of state and thermal relaxation towards the initial radial temperature profile (cf. Equation (3) and Section 3.1). The influence of numerical resolution and mesh refinement on the stresses obtained in model M1 are discussed in the appendix. The same equation of state and thermal relaxation prescription is adopted for the non-isothermal HD model, “N1”, which includes an *enhanced* viscosity to model the angular momentum transport associated with the MRI-induced turbulence that is absent in the HD case. To study the impact of the equation of state (and ultimately radiative transfer processes within the PPD and CPD), we furthermore study a second HD model, “N2”, which does not solve an energy equation, but instead adopts a locally isothermal equation of state where the temperature,  $T$ , is prescribed as a fixed function of cylindrical radius.

For the magnetized disk run, after the parent disk has reached a quasi-stationary turbulent state we gradually insert a planet by smoothly increasing its mass to  $100M_{\oplus}$  over a time scale of roughly three planet orbits. This mass range corresponds to the rapid gas-accretion phase of the core accretion scenario (Papaloizou & Nelson 2005). For the viscous HD runs there is no need to run the parent disk to steady state prior to inserting the planet, so the above procedure is followed without relaxing the disk. Once the planet is fully inserted, the simulations are run until the mass accretion rate onto the planet approaches a quasi-steady state. To give an idea of the numerical expense associated with the complexity of the MHD model, this required 978,600 core hours for simulation M1 alone, amounting to an estimated energy consumption on the order of 100 MWh equivalent of an emission of about 60 tons of  $\text{CO}_2$ .

#### 4.2. General disk morphology

We begin our analysis by presenting general features of the models. In Figure 1 we show midplane slices of the gas density at the end of each simulation. Light colors indicate low surface density, as in the gap region, and dark colors represent high density, tracing the spiral wakes induced by the planet. We note that gap formation in the simulations has not reached completion due to the high computational cost of these runs, so we see that the gap in the direct vicinity of the planet is deeper than at azimuthal positions away from the planet. The material within the co-orbital region executing horseshoe orbits has yet to either diffuse onto orbits that cause it to accrete onto the planet or join the rest of the protoplanetary disk, but eventually this is expected to occur on longer time scales of about a few 100 planet orbits (Nelson et al. 2000), or perhaps longer than this in the presence of dead zone.

The instantaneous cooling in the isothermal model N2 leads to a higher mass and steeper density profile within the CPD, and to a pronounced and tightly wound bi-symmetric spiral as observed in earlier work (e.g. Lubow et al. 1999). In the adiabatic HD model with prescribed cooling shown in panel (b), the spiral arms are less tightly-wound because of warmer temperatures in the CPD. The temperature in the inner regions of the CPD remains at  $T \approx 150$  K in the isothermal run N2. Even though rapid cooling is applied in the non-isothermal

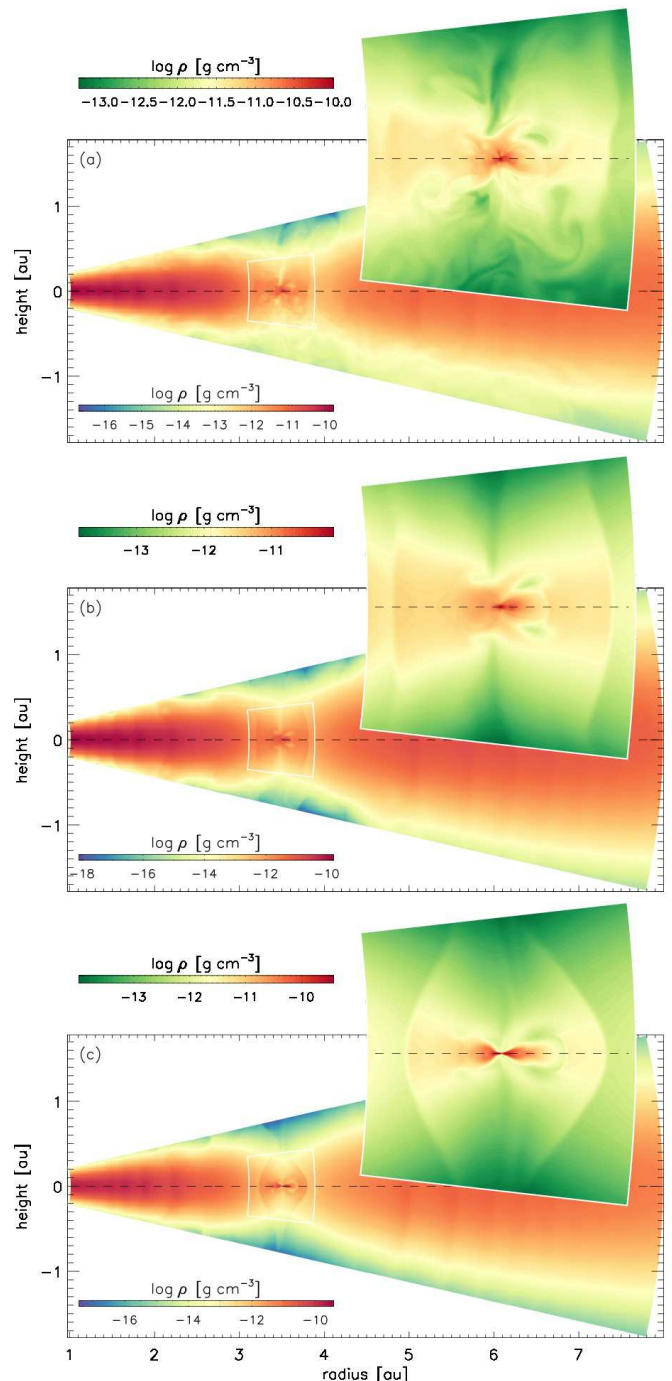


FIG. 2.— Meridional plane showing  $\log(\rho)$  at the planet location (note the separate color bars for the insets). From top to bottom: (a) MHD run, (b) HD run with cooling, (c) isothermal HD run. Under-dense layers above and below the CPD are related to pairs of poloidal vortices.

simulations N2 and M1, temperatures in the inner regions of the CPDs reach  $T \approx 2000$  K for these runs (similar to the values  $T \approx 1500$  K obtained by Klahr & Kley (2006) in their 3D radiation hydrodynamic runs). The mass of the CPD is smaller in run N1 and the density profile is shallower (see Figure 10 below). The flow around the planet is less regular but still laminar, because each fluid element now has its own thermal history leading to moderate pressure fluctuations in the CPD. This changes in the MHD case shown in panel (a), in which the flow pattern becomes turbulent, but otherwise

appears similar to the equivalent HD simulation.

In their study of giant planets embedded in fully-turbulent disks without dead-zones, Nelson & Papaloizou (2003) comment on the fact that the spiral wave structure in turbulent protoplanetary disks has a more washed-out and diffused appearance than observed in laminar disks. This is clearly not the case here in the midplane because the dead-zone contains only relatively low-level density perturbations due to waves propagating from the over-lying active layers. The dominant perturbations are the spiral wakes excited by the planet. At higher, more turbulent latitudes in this disk, however, the planet-induced spirals will have a more diffused appearance. An image of the disk based on the integrated column density would similarly display a more diffused rendering than that shown in Figure 1.

The differences between the isothermal and non-isothermal equation of state become very apparent when looking at poloidal cuts through the simulation domain, presented in Figure 2. Compared to both the HD run N1, panel (b), and the MHD run, panel (a), the CPD is noticeably thinner for the locally isothermal model, N2, shown in panel (c). All three cases, however, agree in the asymmetry between the inner and outer parts of the CPD, with the inner part of the CPD lying nearest to the central star being vertically thicker than the component lying further away. This feature is very likely due to the thermal model that we adopt which assumes that gas lying closer to the star is warmer than that further out (this is true for both the locally isothermal and adiabatic disks with thermal relaxation). In a more realistic model, where the temperature of the CPD is determined by local heating and cooling processes, we suspect that this in-out asymmetry will be less pronounced than displayed by our simulations. We note, however, that in the presence of a gap, a moderately decreasing temperature at the midplane may be expected as one moves out across the gap, because reprocessed stellar radiation from the outer gap edge more directly illuminates the inner half of the gap (Turner et al. 2012).

The overall structure of the CPD is quite similar in the non-isothermal HD and MHD cases, indicating that gravity remains the dominant force (the plasma  $\beta_p$  – defined as the ratio of thermal to magnetic pressure – typically lies between the values 100-1000 in the CPD region, see Figure 13), but it is also clear that the circumplanetary region in the MHD run shows considerably more structure than model N1 due to turbulence. Comparing panels (a) and (b) reveals an inherent limitation in the “enhanced” viscosity prescription that we applied in the HD case: the resolved flow remains laminar, and the stochastic nature of the resulting structures observed in the MHD run cannot be captured in this framework. While this may be tolerable when studying the secular evolution of a PPD, it is probably not sufficient for the purpose of studying dynamical processes occurring in CPDs such as satellite formation where the time dependent structure of the circumplanetary disk may be crucial.

A low-density funnel along the rotation vector of the PPD can be observed in all three simulations. In the two HD simulations, this funnel is always associated with low-angular-momentum material falling in onto the poles of the planet. In the MHD run this is also usually the case, but we have also observed the sporadic occurrence of a (one-sided) magnetically collimated protoplanetary outflow that we will discuss in more detail later in this paper. The sporadic nature appears to be related to the fact that the jet can be disrupted by incoming material accreting through the polar regions.

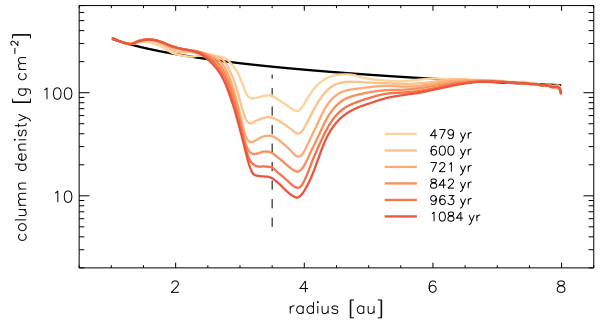


FIG. 3.— Time sequence of the gap opening for the MHD run, M1. Consecutive profiles are for equal time intervals of  $\Delta t = 121$  yr after the planet is inserted. Gap opening is not yet complete at the end of the simulation.

Taking a global view of the simulation results, we can state that significant differences arise in the non-magnetized simulations when moving from an isothermal equation of state to an adiabatic one with imposed cooling, due to the importance of compressional heating associated with gas flowing into the planet Hill sphere. Magnetic fields also play an important role as they transform the circumplanetary flow from one that is essentially laminar to one that is turbulent and highly fluctuating, described later in Sect. 6.4.

## 5. GAP FORMATION

As outlined above, we chose an initial planet mass of  $100M_{\oplus}$ , as this mass puts the planet in the rapid growth phase that we are interested in. It is evident that a combination of tidal torques and gas accretion onto the planet lead to the formation of a significant gap within the PPD. Considering the gap opening criteria that the tidal torque must overcome the effective viscous torque ( $q \geq 40/\mathcal{R}_e$ , where  $q = M_p/M_*$  and  $\mathcal{R}_e$  is the Reynolds number) and the Hill sphere radius of the planet must exceed the local scale height<sup>3</sup>, we find that a  $100M_{\oplus}$  planet just fails to meet the second criterion, but satisfies it when its mass grows above  $110M_{\oplus}$ . The first criterion is fulfilled for planet masses exceeding  $60M_{\oplus}$  when  $\alpha = 2 \times 10^{-3}$  and  $h = 0.05$ , so the opening and maintenance of a gap is expected in the simulations. We note that low mass planets are known to open modest gaps or surface density depressions in disks due to shock dissipation of their spiral wakes (Goodman & Rafikov 2001; Muto et al. 2010), so the above gap-opening criteria should not be interpreted too rigidly.

The gap opening process is illustrated in Figure 3, where we plot radial profiles of the disk surface density in regular intervals of  $\Delta t = 121$  yr, corresponding to roughly 20 orbital times at the planet location. While the gap has not reached a fully stationary state, the deepening of the gap is clearly slowing down towards the end of the simulation. Moreover, there is a trend towards deepening the outer half of the gap, which is also visible in Figure 1. This arises primarily because the disk is cooler just outside of the planet location compared to the corresponding region just interior to it. Waves excited at the outer Lindblad resonances are therefore more nonlinear than their inner Lindblad resonance counterparts. The density contrast between the edge and the gap is roughly 20-30, which is a factor of 2-3 deeper than reported for the local shearing-box models of Machida et al. (2008). The periodic nature of shearing box simulations may reduce the depth of the gap, an effect that is avoided in our global simulations.

<sup>3</sup> i.e.,  $R_H > H$ , which is equivalent to the requirement that the disk response to the planet gravity be nonlinear (Lin & Papaloizou 1993)



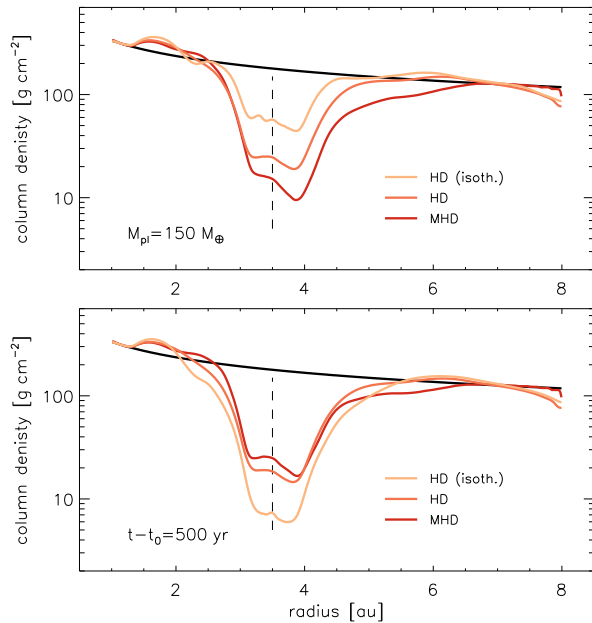


FIG. 4.— Radial gap profiles (including the mass contained in the CPD). *Top*: for constant planet mass of  $M_p = 150M_\oplus$ . *Bottom*: at constant time  $t - t_0 = 500$  yr, where the momentary planet masses are 143, 153, and  $196M_\oplus$  for models M1, N1, and N2, respectively. The solid black line indicates the initial profile; the dashed line shows the planet position.

We remark that their simulation had a similar mass planet ( $0.4M_J \simeq 127M_\oplus$ ), which was embedded in an inviscid disk without magnetic fields or turbulence.

In Figure 4, we show a comparison of the gap structure between the different models. Because of the different accretion rates (see discussion in Sect. 7.1 below), we perform this comparison in two different ways: at constant planet mass of  $M_p = 150M_\oplus$  (upper panel), and at constant time  $t - t_0 = 500$  yr after the insertion of the planet (lower panel). Gap opening proceeds fastest in the isothermal-HD case, N2, presumably due to the more efficient mass growth of the planet in this setup. At a given planet mass, the model M1 shows the deepest gap, followed by the equivalent HD model, N1.

Comparing the simulation results at a fixed evolution time, our non-isothermal MHD and HD runs have quite comparable gap structures (lower panel of Figure 4). There is a noticeable difference in the gap edges, with the MHD model having a higher density inner edge, and a lower density outer edge compared to the HD model. While this may have implications for the detailed torque balance experienced by the planet, a detailed examination of this issue is probably not warranted due to the fact that none of the simulations have formed a steady-state gap. Gap opening has been studied extensively in fully MRI-active disks. While early studies neglected the vertical stratification (Nelson & Papaloizou 2003; Winters et al. 2003; Papaloizou et al. 2004) this has recently become possible to include (Uribe et al. 2011). These studies generally find that a giant planet embedded in an MRI-turbulent disk opens a wider gap than one embedded in an equivalent HD simulation that utilizes the  $\alpha$  model for viscosity, and the upper panel of Figure 4 provides some support for this. We caution, however, that direct comparison with these previously reported trends is difficult because the planet in this paper has a time dependent mass due to accretion, unlike the previous studies that used a fixed mass.

### 5.1. Consequences of evolving ionization fraction

Formation of a gap reduces the column density in run M1, increasing the midplane ionization fraction of disk material there through increased penetration of X-rays and cosmic rays. In essence we observe the dead-zone in the vicinity of the planet being ignited into a turbulent state by gap formation. As we have discussed above, gap formation does not run to completion in this simulation, so we find that it is primarily the upper and intermediate layers of the disk in the gap that share common characteristics with the MRI-active surface layers of the rest of the PPD. The gap is deepest in the close vicinity of the planet (i.e. in a wedge of  $\phi \simeq \pm\pi/8$ ), and the magnetic Reynolds number,  $Rm \equiv c_s H / \eta$ , has high values in the range  $10^4 - 10^5$  there. At the same time, the Ohmic Elsasser number,  $\Lambda \equiv v_A^2 / (\Omega \eta)$ , with  $v_A$  the Alfvén speed associated with the vertical field, is well above unity. Accordingly, we find this region in particular to be in a turbulent state all the way down to the midplane. Values of  $\beta_p$  are in the typical range for active MRI. As one moves away from the planet position around the orbit the characteristics of the flow change. Particularly in the midplane, and away from the planet,  $Rm$  drops to values as low as 100, which is generally insufficient for sustained MRI (Oishi & Mac Low 2011). Moreover,  $\Lambda$  becomes smaller than unity; in agreement with linear theory the flow remains laminar in these regions. At the same time, the plasma there is only very weakly magnetized with  $\beta_p \sim 10^5$ .

Taking a global view of the flow in the protoplanetary disk and gap region, we can say that gas accretes through the disk toward the planet mainly *via* the upper active regions. As gas enters the gap it is pulled down by the star’s gravity and toward the planet by its gravity. The low density there allows strong coupling between the gas and the predominantly azimuthal magnetic field such that the field is advected with the fluid into the gap, where it helps to sustain the MRI. Because our simulations do not allow gap formation to run to completion, gas within the gap region at azimuthal locations away from the planet remains laminar at the midplane. On longer time scales, however, we would expect these regions to also become evacuated such that the MRI could be sustained there also. The end result would be a protoplanetary disk with active surface layers and laminar midplane region far from the planet, but a magnetized and turbulent gap in the planet’s vicinity through which material passes as it flows into the planet Hill sphere.

### 5.2. Consequences of accreting from a layered disk

The feeding of gas into the gap region from the surface layers may have important consequences for the chemistry and dust content of the gas that eventually accretes onto the planet, as dust settling and sequestration in the dead-zone may reduce the heavy element content of this gas as it accretes through the disk. Possible implications of this are discussed in Sect. 8.

An interesting consequence of accretion through a gap in a layered disk is that the gas flow through the surface layers into the gap should be able to continue relatively unimpeded by tidal truncation of the disk even for relatively massive planets, because the magnetic stresses and associated  $\alpha$  values in the upper layers tend to be very large (i.e.  $\alpha > 0.1$ ). As such, these disk layers will not satisfy the viscous gap opening criterion discussed above, and should continue to feed the planet as its mass grows, albeit at a moderate rate because of the low densities in the upper layers. As we discuss later in the paper,

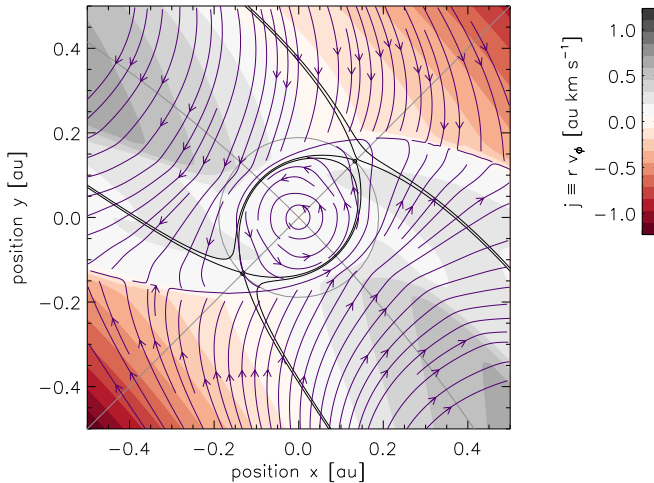


FIG. 5.— Time-averaged flow field (arrows) and specific angular momentum (color coded) for a midplane slice of the isothermal HD model. Averages are taken over  $\sim 4$  planet orbits after the planet has reached a mass of  $150M_{\oplus}$ .

the accretion rates observed in the viscous hydrodynamic runs N1 and N2 show a tendency to continuously decrease as the planet mass increases and the gap deepens. Run M1, however, appears to reach a steady accretion rate that is higher than observed in the laminar runs by the end of the simulation (see Figure 16), apparently for the reason just described.

## 6. THE CIRCUMPLANETARY DISK

We now discuss the features of the flow in our models on scales appropriate to the planet Hill sphere radius. We begin by describing the horizontal flow features in the midplane, before examining the flow pattern in the meridional plane. We discuss and compare the integrated properties of the circumplanetary disks that arise in all of our simulations, before focusing on the details of the flow that arise in the MHD simulation M1.

### 6.1. Horizontal flow features in the midplane

Within the Hill sphere (where the gravitational force of the planet dominates), we observe the formation of a circumplanetary disk in all simulations as a consequence of the approximate conservation of (specific) angular momentum,  $j \equiv r v_{\phi}$  (with respect to the planet’s position).

In Figure 5 we plot the time-averaged specific angular momentum of the flow region near the planet for the locally-isothermal run N2. Superimposed streamlines show that the flow has a high degree of symmetry. Marginally bound trajectories closely follow the Roche lobe (equipotential surfaces through L1, L2 are shown as black lines), indicating that the flow is only weakly affected by pressure forces. The flow within the CPD is nearly circular at this time, but is observed to become more distorted at late times as discussed in Sect. 7.2. In comparison, the averaged flow field appears less symmetric in the simulation with an adiabatic equation of state and thermal relaxation towards the initial temperature (upper panel of Figure 6). Unlike in the previous case, the circulating flow appears to extend beyond the Roche lobe, and shows some level of distortion. This is partly due to the fact that the upper panel in Figure 6 corresponds to a later time when gap formation is more developed; we generally find that the CPD flow becomes increasingly distorted as the simulations evolve and gap formation becomes more pronounced. The distortion is apparently also amplified by the enhanced

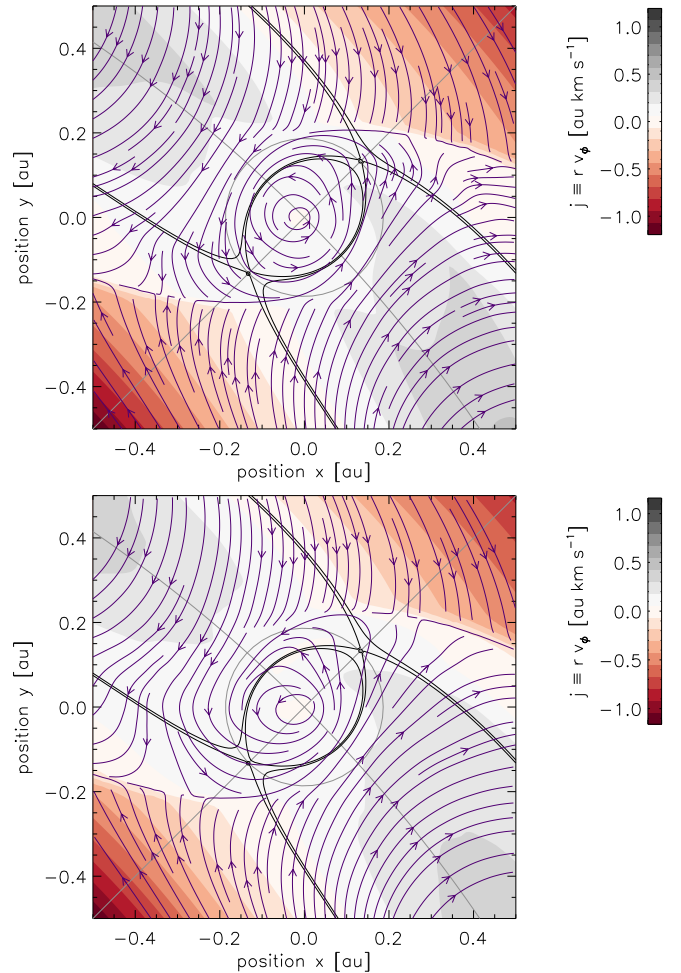


FIG. 6.— Same as Figure 5, but for the non-isothermal HD model (top), and the MHD model (bottom panel).

pressure forces present in run N1, combined with the in-out asymmetry that the circumplanetary material displays because of the radial temperature profile imposed on the gas.

This trend of reduced order in the fluid trajectories is enhanced substantially when looking at the MHD case, shown in the lower panel of Figure 6: here the flow within the Hill sphere is significantly distorted and less symmetric, presumably due to the combined effect of pressure and magnetic forces. Notably, the flow within the CPD appears to have a non-negligible eccentricity. Magnetic field lines (not shown) are dominantly azimuthal (with respect to the PPD) outside the horseshoe region and moderately compressed in the spiral arms; notably  $B_{\phi}$  has opposite sign in the inner and outer part of the PPD. In the vicinity of the planet orbit (the horseshoe region and just beyond), field lines are generally aligned with the flow, with the exception of the post-spiral shock region where angles up to  $90^{\circ}$  are obtained. Within the CPD, the field lines follow the winding of the spiral shocks. Overall the field morphology is consistent with that described by Nelson & Papaloizou (2003).

### 6.2. Poloidal and three-dimensional flow features

During the early phase of evolution, prior to pronounced gap formation, we find that the flow field observed in poloidal slices in the isothermal run N2 is qualitatively very similar to the highly symmetric renderings shown in figure 5 of Machida et al. (2008) and figure 4 of Tanigawa et al. (2012).

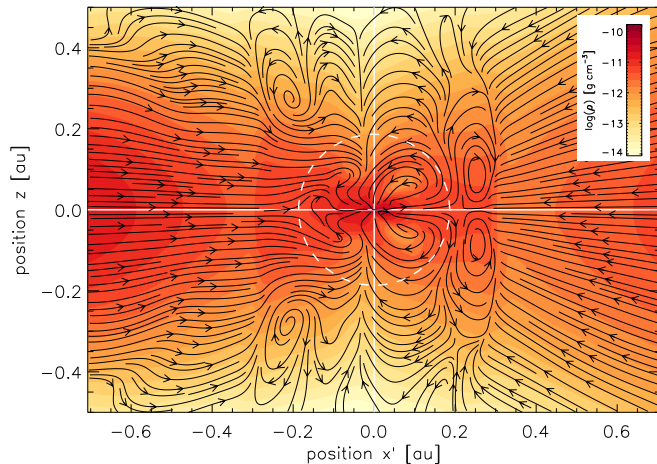


FIG. 7.— Projected flow field in the vertical plane connecting the planet with the star. Small vortical return flows within the Hill radius (dotted) are associated with under-dense regions already seen in Figure 2. Note the strong vortex pair adjacent to the outer spiral arm.

This flow consists of inflow toward the planet at high latitudes, and outflow toward the L1 and L2 points near the CPD midplane. During late times, when gap formation is more developed, we find that the flow symmetry breaks down and becomes similar to that displayed by the non-isothermal HD run N1, for which we plot poloidal flow lines near the end of the simulation in Figure 7. Within the outer half of the Hill sphere, material is centrifugally spun-out towards the L2 point near the CPD midplane and then recycled into the vertical accretion flow along the vertical axis of the planet. Unlike at early times, and in the (intrinsically symmetric) local simulations of Machida et al. (2008), this is markedly not the case on the side of the CPD facing the star, where we only observe inflow. This difference is also clearly seen in Figures 17 and 18 in Section 7.2 below.

Outside the Hill sphere, the non-isothermal flow shows substantially more complex features than the ones seen for an isothermal gas. Most notably, there is a pair of vertically elongated poloidal vortices sitting right outside, above and below the L2 point. These vortices possibly have their origin through baroclinic generation of vorticity (via the  $\nabla P \times \nabla \rho$  term) in the vicinity of the spiral shock. A similar but weaker (and more widely separated) pair is seen on the side close to the star. Note that the apparent ending of stream lines outside the vortices is a projection effect. Near the spiral shock, the flow abruptly changes direction, pointing into/out-of the plane shown in Figure 7.

A three-dimensional volume rendering of the flow field of model N1 is attempted in Figure 8, where we recognize the outer vortex pair (the slice from Figure 7 passes through the left-right diagonal here). These flow lines are traced from the vicinity of the planet in the CPD, and demonstrate that inflow primarily occurs from high latitudes and not along the midplane of the CPD. This feature of the accretion flow is discussed in greater detail in Sect. 7.2. The flow structure becomes even more tangled-up in the MHD case, which is not shown here. A detailed discussion of the intrinsic variability seen in this run is presented in Sect. 6.4 below.

### 6.3. Integrated properties of the CPDs

In Figure 9, we compare time-averaged angular momentum profiles within the CPD midplane of the three main models. Differences, due to additional radial pressure support,

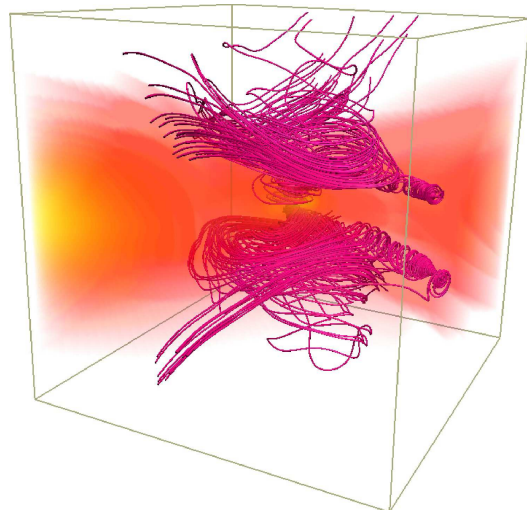


FIG. 8.— Backward extrapolation of stream lines passing through the close vicinity of the planet. Final snapshot from the non-isothermal HD model. The size of the cube is 1 au, and the left corner points towards the star. For orientation, the gas density is shown. Adjacent to the outer spiral shock, a pair of counter-rotating vortices is visible.

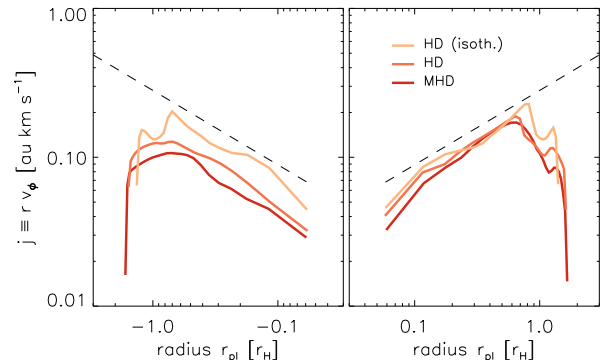


FIG. 9.— Time-averaged (as in Figure 5) specific angular momentum profile within the CPD midplane along the ray connecting to the star. The left (right) panel shows the half of the CPD facing towards (away from) the star. Keplerian rotation is indicated by the dashed line.

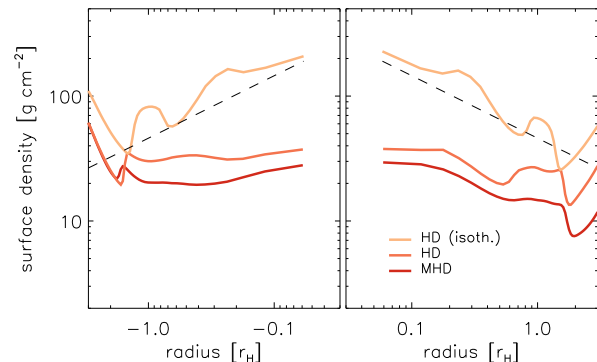


FIG. 10.— Time-averaged surface density profiles for the three cases. Lines represent a radial slice through the CPD midplane. The dashed line indicates a surface density profile  $\sim r^{-0.5}$ .

are more pronounced for the part of the disk closer to the planet. This is consistent with the geometrically thicker inner disk seen in the insets of Figure 2. As expected in the absence of strong pressure gradients (that might arise because of compressional heating near the planet), the isothermal model is closest to the Keplerian rotation profile (dashed line). In the MHD model, the CPD rotates the slowest, indicating that

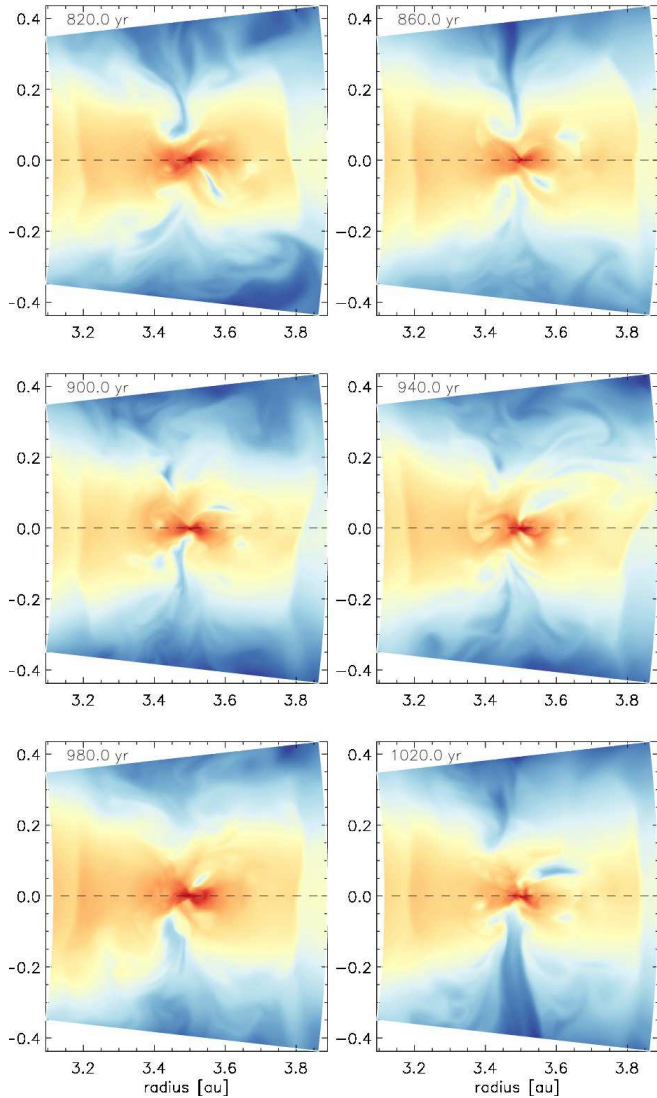


FIG. 11.— Time sequence of edge-on slices of the gas density for the MHD model illustrating the stochastic, heavily time-varying nature of the CPD. While the low-density, tornado-like structures (roughly aligned with the rotation axis of the CPD) are associated with inflow, the funnel seen in the lower half of the last panel is in fact a collimated jet-like outflow (see Fendt 2003).

magnetic forces, at least at some level, contribute to the overall structure of the disk. Estimating the size of the CPD according to the radius at which the specific angular momentum begins to turn, we find the CPD extends to about half the Hill radius, which is similar to but slightly larger than the CPDs reported in other studies where values of one-third of the Hill sphere radius (Ayliffe & Bate 2009a; Machida et al. 2008; Tanigawa et al. 2012) or  $0.4r_H$  (Martin & Lubow 2011) have been estimated. These estimates are influenced by the disk temperature because of the role of pressure forces at the CPD outer edge, and also by the properties of the inflowing gas such as its angular momentum, so we believe our results are consistent with those obtained in previous studies.

The radial surface density profile of the CPDs from all models is shown in Figure 10. Unlike the two non-isothermal models, the isothermal HD model shows a cusp-like inner disk structure, as well as pronounced spiral features (cf. Lubow et al. 1999) leading to peaks in the surface density profile. We find the profile is close to a  $\sim r^{-0.5}$  dependence,

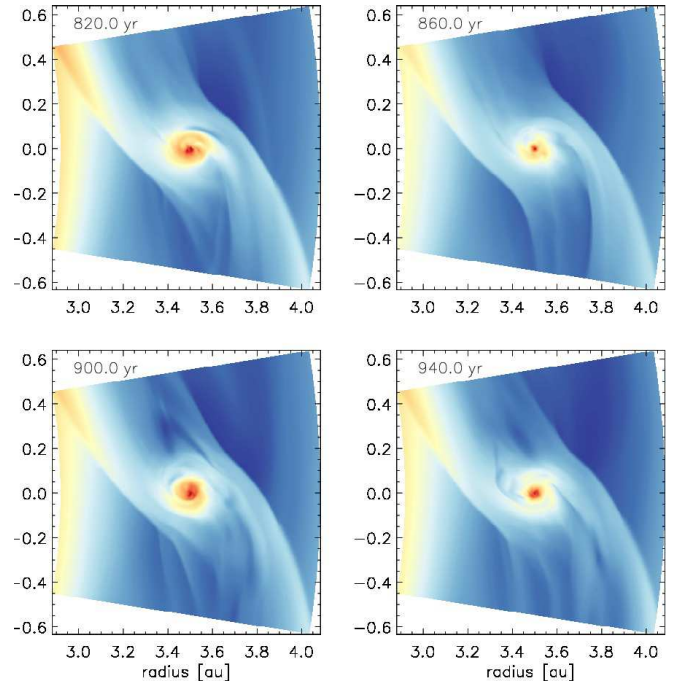


FIG. 12.— Similar to Figure 11, but for midplane slices of the gas density, which is shallower than the  $\sim r^{-1.5}$  dependence reported by Tanigawa et al. (2012). The reason for this minor discrepancy is likely to be our adoption of a larger sink hole radius. When applying a non-isothermal equation of state, we find lower and nearly constant surface densities, and much weaker spiral features due to the higher temperatures. The inclusion of magnetic field leads to a further reduced disk mass. Generally, the observed surface densities are in the range of the “gas-starved” scenario of Canup & Ward (2002, 2006), which is significantly lower than in the “minimum mass” models of Mosqueira & Estrada (2003). If we integrate the mass contained within the Roche region (black lines in Figures 5 and 6), we obtain  $0.041M_\oplus$  for model M1,  $0.063M_\oplus$  for model N1, and  $0.196M_\oplus$  for model N2, respectively. These numbers should be contrasted with the the Jovian satellite system mass  $\simeq 0.067M_\oplus$ , which if augmented to solar abundance would imply the presence of  $\simeq 7M_\oplus$  of gas.

#### 6.4. Time-dependent morphology in the MHD case

Having inter-compared the gross properties of the CPD regions for our three runs, we now consider the detailed and time-dependent structure of the CPD region for the magnetized run M1. We leave discussion about the geometry of the actual accretion flow onto the planet until Sect. 7.2. In Figure 11 we present a series of snapshots showing vertical slices of the density, demonstrating the substantial time-variability of the accretion flow in this region because of the turbulence in the gap that feeds material into the planet Hill sphere. We see low-density patches within the CPD that are connected with the poloidal vortices that develop within the flow, described in Sect. 6.2 above. A similar level of temporal variation is seen in the sequence of midplane slices shown in Figure 12.

We plot a vertical slice through the circumplanetary disk region showing the value of the time-averaged plasma  $\beta_p$  value in Figure 13. The CPD is relatively weakly magnetized, with  $\beta_p$  typically in the range  $10^2$ - $10^3$ , while material falling in through the funnel-shaped regions above and below the planet are characterized by equipartition-strength magnetic fields.

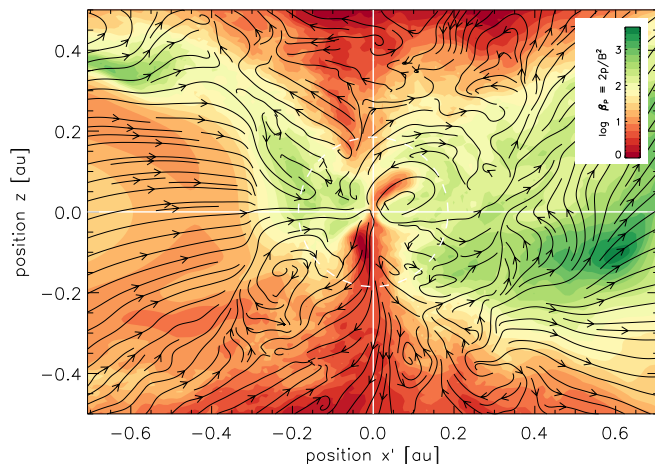


FIG. 13.— Radial-vertical slice of the logarithm of the plasma parameter,  $\beta_P \equiv 2p/B^2$ , and projected magnetic field lines. Averages are taken over eight planet orbits at the time corresponding to the last panel in Figure 11.

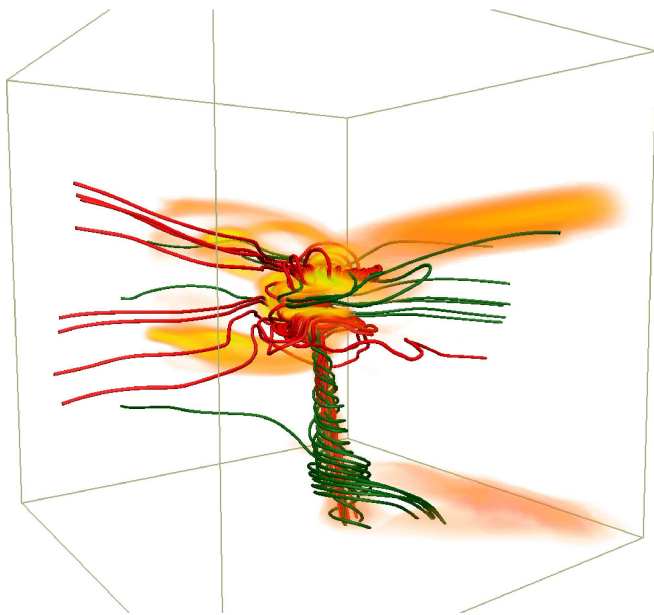


FIG. 14.— Volume rendering of the single-sided, cone-shaped outflow seen at one instance in time during the MHD run. Selected flow lines passing through the vicinity of the planet (red) are shown within a cube of 1.5 au (with the viewing direction being very similar to Figure 13 above). Draped around them is a helical magnetic field (green lines) leading to collimation of the outflow *via* the magnetic hoop stress. Shaded volumes indicate regions of strong Ohmic dissipation.

The field topology in this region can very crudely be described as follows: the large-scale azimuthal field in the MRI-active layers is dragged downwards with the accretion flow. Within the Roche lobe, the cusp of the now V-shaped field lines is twirled-up by the circular flow around the planet, producing a helical field topology. One consequence of this field evolution appears to be the launching of a relatively diffuse, accelerated wind from the conical regions above and below the circumplanetary disk. More localized vertical outflows (e.g. note the mushroom-shaped bow shock seen in the upper half of the fourth panel in Figure 11) appear sporadically during the simulation but generally do not display high levels of collimation and are quickly disrupted by the vigorous MRI turbulence.

In contrast to this rather diffuse disk wind just described, the MHD simulation did produce one episode of sustained,

collimated outflow as shown in the last panel of Figure 11. This is more dramatically illustrated by the volume rendering in Figure 14 which shows both the fluid streamlines and magnetic field topology. This collimated outflow lasted for a period of about four planet orbits before it was squashed by infalling material. Unfortunately, the non-aligned mesh geometry and intrinsic variability make the outflows hard to access quantitatively, so the driving mechanism cannot be pinned down definitively, but it is clear from the twisted field wrapped around the outflowing gas that the protoplanetary jet seen in Figure 14 is collimated by magnetic hoop stresses. Given the importance of magnetic field advection and rotation in the vicinity of the planet, our suggestion that the outflow is magnetocentrally driven is well-motivated, but speculative at the present time. It is possible that field winding generates sufficient magnetic pressure to launch the jet at its base instead, although this is doubtful because field amplification in the circumplanetary disk is damped efficiently by Ohmic diffusion (see volume rendering in Figure 14). A deeper analysis of protoplanetary jet launching will be presented in a future publication. We note that CPD jets have been predicted on theoretical grounds by Quillen & Trilling (1998) and Fendt (2003), and they have been observed in local shearing box simulations by Machida et al. (2006). The physical set-up in this latter study was quite different from the one we consider here, however, because we initiate the simulation with a weak magnetic field, and strong local fields are built up in the vicinity of the planet by gas accretion and associated advection of magnetic field from the surrounding PPD at late times in the simulation. The study by Machida et al. (2006), however, employed an equipartition strength vertical magnetic field, leading to the formation of a well-defined bipolar outflow shortly after the simulation was initiated. Although interesting as phenomena in their own right, there is no evidence at present that the launching of a CPD jet has a significant influence of the growth of the planet. Examination of the gas accretion rate onto the planet does not indicate that it is influenced significantly during the time of strongly collimated jet launching, implying that momentum and energy injection into the surrounding infalling envelope is not an important process here. A scenario in which wind or jet launching from a CPD may be important for determining the accretion rate onto the planet corresponds to a scaled-down version of the picture presented by Bai & Stone (2013), where the combined effects of Ohmic resistivity and ambipolar diffusion cause angular momentum transport and mass accretion in a protoplanetary disk to arise through the launching of a magnetized wind. If such a scenario also applies to accretion onto a planet through a CPD, then wind launching will be central to determining the accretion rate onto the planet.

The stochastic nature of the accretion flow into the planet Hill sphere implies that the angular momentum vector of the CPD material should not maintain a constant orientation. This expectation is confirmed by Figure 15 which shows the time evolution of the angle between the angular momentum vector and the vertical axis calculated for all material inside the planet Roche lobe for the various simulations. As expected, we see that both of the HD runs maintain a reasonably constant direction for the CPD angular momentum vector after an initial period of relaxation, with the tilt angle remaining  $< 1^\circ$ . The MHD run, however, shows high levels of variability over the full time span of the run, with tilt angles reaching up to  $15^\circ$ . Although this measurement applies to all material in the Roche lobe, and not just the material in the well-defined

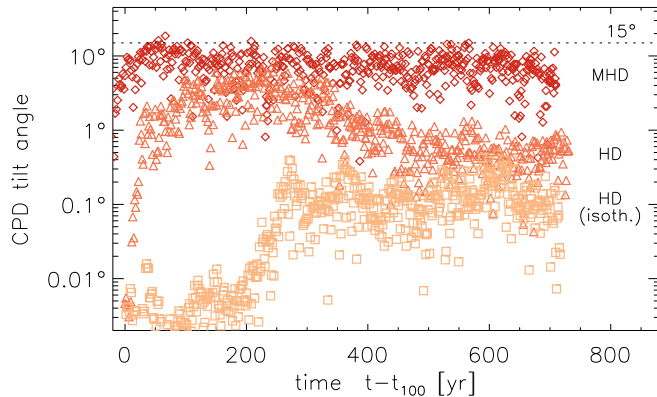


FIG. 15.— Tilt angle of the mean angular momentum vector (of all the material within the Roche lobe) as a function of time  $t - t_{100}$ , i.e., after each planet has reached its initial mass of  $100M_{\oplus}$ .

CPD confined to less than half the Hill radius, it seems very likely that the inner part of the CPD close to the planet will experience substantial disturbance that causes it to tilt and precess. In particular, stochastic accretion of material with different specific angular momenta will cause local warping on orbital time scales that may excite bending waves that propagate through the circumplanetary disk (e.g. Papaloizou & Lin 1995; Larwood et al. 1996), with interesting consequences for its dynamical evolution and the formation of regular satellite systems in the inner regions. Indeed, we speculate that when all other things are equal, a higher mass planet will host a circumplanetary disk that is subject to reduced levels of perturbation in the inner satellite forming regions compared to a lower mass planet, by virtue of the strength of the local gravitational field relative to the external perturbing forces that are independent of the planet mass. This may be of relevance when comparing the regular satellite systems of Jupiter and Saturn, where the Jovian system clearly is more substantial than Saturn’s.

At late times during the MHD simulation, the component of the CPD that we model is itself marginally unstable to the MRI – i.e., according to the Elsasser number,  $\Lambda \sim 0.2 - 20$ , based on Ohmic diffusivity alone. We would predict this to be the case from the surface density values displayed earlier in Figure 10. The penetration depth of X-rays is  $\sim 9 \text{ g cm}^{-2}$  and for cosmic rays it is  $\sim 90 \text{ g cm}^{-2}$ . Allowing for partial attenuation of these ionizing sources by overlying material in the gap region, we would predict that the circumplanetary disk is MRI-active based on the measured column densities (but see Turner et al. 2013, for a more detailed assessment). The magnetic Reynolds number is rather low ( $R_m \simeq 100 - 1000$ ), which implies that a relatively strong vertical net flux will be required to facilitate sustained MRI. Build-up of strong fields through advection into the Hill sphere, and subsequent amplification of the toroidal component by differential rotation, is opposed by Ohmic diffusion, so we might reasonably expect the disk to attain a marginal state of MRI.

Given the stochastic nature of the accretion flow and the associated tilting and warping of the disk, it is hard to assess whether the CPD in our MHD simulations is in fact laminar or MRI-turbulent. Within the restrictions of our diffusivity model, and based on the associated dimensionless numbers, the latter possibility can certainly not be excluded. If we, on the other hand, estimate the vertical wavelength of the fastest growing (ideal) MRI mode, we find a typical value of  $\lambda_{\text{MRI}} \simeq 5 \times 10^{-3} \text{ au}$  – approximately coinciding with the

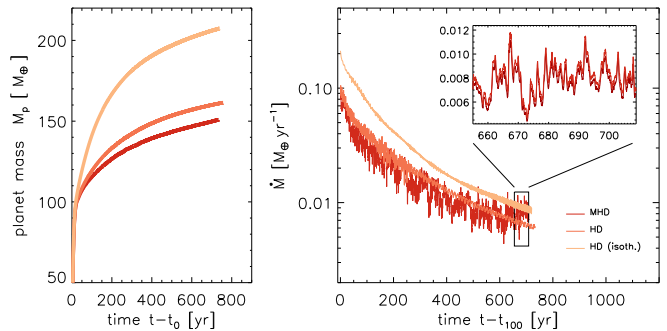


FIG. 16.— *Left*: Evolution of the planet mass after insertion ( $t_0$ ). *Right*: Mass accretion rates after  $100M_{\oplus}$  are reached ( $t_{100}$ ). The inset additionally shows (for the MHD case) the mass accretion rate into a sphere with  $2r_{\text{acc}}$ , demonstrating that the flow near the sink is essentially ballistic.

Nyquist frequency of our finest grid (and hence falling short of the *minimal* resolution requirement by roughly a factor of five). In view of this issue, and regarding a possible existence of a disk-wind and/or magneto-centrifugal jet, even better resolved mesh-refined models are certainly called-for.

## 7. THE ACCRETION FLOW ONTO THE PLANET

As has been pointed out in various previous studies (e.g. Klahr & Kley 2006; Machida et al. 2008; Shabram & Boley 2013), the accretion flow onto the planet in a laminar disk is genuinely three-dimensional. This is also confirmed by all our models which develop complex flow structures in both the vertical and horizontal directions, with inflow toward the planet arising primarily from high latitudes. In agreement with previous high-resolution studies of the accretion flow onto a giant planet from laminar, inviscid, isothermal disks (Machida et al. 2008; Tanigawa et al. 2012), we also find that material flows *away* from the planet near the midplane of the CPD and toward the planet from higher latitudes in our locally isothermal run. Outflow away from the planet near the midplane of the CPD is also observed in the two non-isothermal runs, although the situation in these runs is less clear-cut.

### 7.1. Mass accretion rates

Before discussing the complex geometry of the accretion flow onto the planet we consider the total accretion rates that are produced by the simulations. The left panel of Figure 16 shows the evolving planet mass for the three models.<sup>4</sup> The mass accretion rate into the sink particle is plotted in the right panel of the same figure. The inset shows a magnification of the late accretion phase in model M1. The additional (darker) line shows the mass flux through a spherical surface with twice the radius compared to the actual “sink” region, within which gas is removed from the domain. We remind the reader that the constant sink hole radius equals 5% of the Hill sphere radius of the initial planet mass  $100M_{\oplus}$ . The minimal offset between the curves demonstrates that the mass flux toward the planet is essentially constant near the accretion sink, indicating that the flow of gas into the sink hole is not retarded by any processes occurring in this region. For the magnetized model, after 500 yr, we reach a quasi-stationary state, for which we infer a mass accretion rate of  $(8.0 \pm 1.4) \times 10^{-3} M_{\oplus} \text{ yr}^{-1}$ . In other words, a Saturn-mass planet can grow to become a

<sup>4</sup> Note that we artificially enhance the mass accumulated by the planet by a factor of four to speed-up tidally-induced gap opening. The reported accretion rates, however, reflect the actual gas flow onto the planet and do not include this factor of four enhancement.

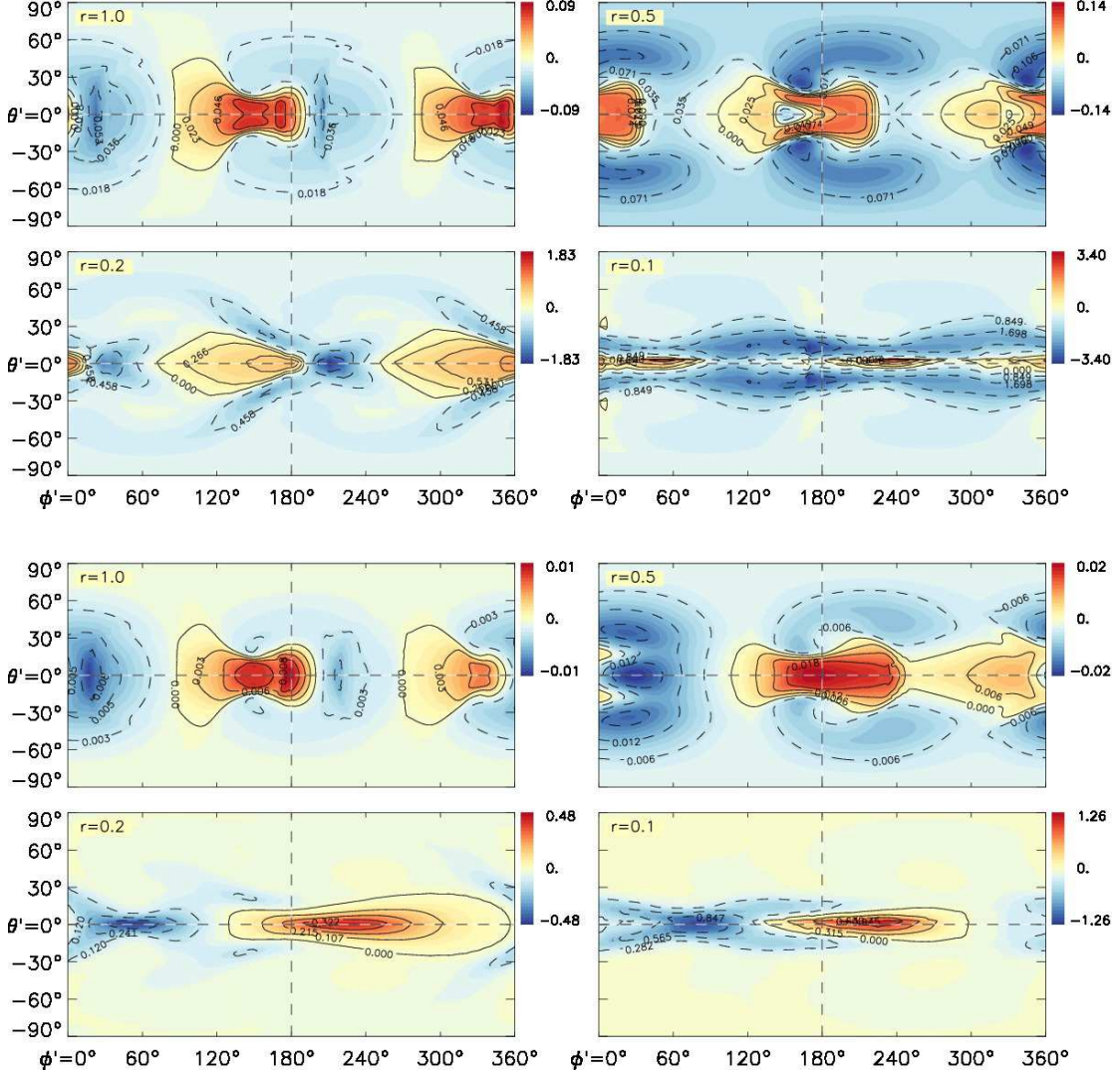


FIG. 17.— Angular distribution of mass flux ( $\rho v_r$ ) into spherical shells around the planet (with  $r = 1, 0.5, 0.2,$  and  $0.1$  Hill radii) for the isothermal HD case at early times (top four panels), and at the end of the simulation (bottom four panels). The coordinates  $(\theta', \phi') = (0, 0)$ , and  $(0, 180)$ , correspond to the sub-solar and anti-solar points, respectively. Inflow is represented by negative values.

Jovian mass within  $\sim 25,000$  yr, a small fraction of the expected disk life-time. In comparison, the total Maxwell stress measured within the CPD is inferred as  $\alpha_M \simeq 0.01$ , translating into an estimated accretion rate of roughly  $10^{-3} M_{\oplus} \text{ yr}^{-1}$ , indicating that probably only a fraction of the mass is actually delivered *via* viscous transport within the disk.

In the other two models, the accretion rate still drops, presumably since gap formation has not completed yet, and there is no MRI-active surface layer with large stresses replenishing material into the gap region. It is evident, however, that contraction of gas onto the planet is more efficient in the locally-isothermal model which lacks compressional heating. Even though we apply cooling on the local dynamical time scale to material deep in the planet Hill sphere in the non-isothermal models, compressional heating influences the dynamics significantly through the build-up of a central pressure gradient, with consequent reduction in the accretion rate. As described earlier in Sect. 4.2, the temperature in the non-isothermal runs reaches values of  $T \simeq 2000$  K in the vicinity of the planet despite the rapid cooling applied there, whereas in the locally isothermal run it remains fixed

at  $T \simeq 150$  K. It is clear that in addition to consideration of MHD processes, an *accurate* model of planetary accretion also needs to account for the influence of radiation transport on the infalling material, even during the runaway growth phase of giant planet formation. Nonetheless, the accretion rates between all models vary by less than a factor of two at the end of the simulation when a quasi-steady state has been reached, indicating that qualitatively the results are in agreement regarding rapid gas accretion onto a growing Saturn-mass planet. We conclude that the adoption of two different equations of state induces only a moderate change in the medium-term accretion rates, in agreement with previous analyzes (e.g. Ayliffe & Bate 2009b; Machida et al. 2010). In particular, we note that Machida et al. quote accretion rates of  $(6-18) \times 10^{-3} M_{\oplus} \text{ yr}^{-1}$  in their discussion, in excellent agreement with our results.

Unlike in the viscous hydrodynamic runs, the accretion in model M1 is stochastic, showing variation by a factor of two over time scales  $\approx 5$  yr. In terms of the average accretion rate, however, the non-isothermal HD and MHD runs produce very similar values. The MHD run produces a slightly smaller

accretion rate during early phases, when magnetic pressure effects within the Hill sphere seem to moderately impede accretion, but at later times when a significant gap has formed the accretion rate for this run levels-off at a higher value than observed for the HD run. As discussed above, this latter effect seems to be due to the large magnetic stresses operating in the MRI-active regions near the PPD surfaces that are not present in a viscous model with constant  $\alpha$ . What is clear from these simulations is that magnetic effects within a semi-realistic protostellar disk model do not provide a barrier to planetary gas accretion on scales larger than 5% of the Hill sphere radius. As far as we can tell from our simulations, giant planets can accrete substantial gaseous envelopes within  $\sim 3 \times 10^4$  yr, in broad agreement with earlier studies of non-magnetized disks.

### 7.2. Details of the accretion flow geometry

Given the complex flow structure in the planet Hill sphere reported here and in previous studies, it is interesting to look at the spherical distribution of the mass flux toward the planet and to compare it with the laminar, inviscid, isothermal models of Tanigawa et al. (2012). This is done in Figure 17, where we look at the mass flux through shells centered around the planet arising in run N1 (cf. figure 5 in Tanigawa et al. 2012, note however the different set of radii, owing to the lower resolution in our global model compared with their shearing box). Mass fluxes are averaged over approximately one planet orbit, and our convention is such that outflow corresponds to positive values (red), and accretion is indicated by negative values (blue). The top four panels display the mass flux onto the planet after  $t \simeq 20$  orbits when its mass equals  $150M_{\oplus}$ . These are comparable with Tanigawa et al. (2012) because their model ran for  $\simeq 25$  planet orbits, leading only to moderate gap formation. The bottom four panels correspond to the end of the simulation when the planet mass moderately exceeds  $200M_{\oplus}$  and gap formation is more pronounced.

Considering the early evolution first, we see that the first panel, at  $r = r_{\text{H}}$ , matches well with the one from Tanigawa et al. (2012). Material flows into the Hill sphere at two diametrically opposite longitudes  $\sim 20^\circ$  in the counter-clockwise direction (when viewed from above) from the L1 and L2 points, respectively. The pronounced  $m = 2$  structure indicates that material also leaves the Hill sphere close to the Lagrange points. The region of inflow seems to be rather loosely defined while the corresponding outflow is more focused, due to the influence of the spiral wake induced by the planet. We remark that the spherical  $r = r_{\text{H}}$  surface is somewhat misleading in that the true shape of the Roche lobe is closer to a rugby ball than to a football (this is evident in Figure 5). We conclude that the flow pattern seen in the first panel of Figure 17 hence reflects the horseshoe orbits entering and leaving the spherical surface at  $r = r_{\text{H}}$ , which is of little significance when considering accretion onto the planet. For the remaining three panels we find a qualitatively similar distribution as in Tanigawa et al. (2012). At all radii the mass fluxes show a clear  $m = 2$  structure related to the spiral features observed in the CPD, again in agreement with Tanigawa et al. (2012). At  $r = 0.5r_{\text{H}}$  inflow occurs at high latitudes and outflow arises around the midplane region at latitudes between  $\theta' \simeq \pm 30^\circ$ . On scales of  $r = 0.1r_{\text{H}}$  there is a noticeable flattening of the disk toward the midplane because the near-constant temperature leads to a flaring CPD structure.

The lower four panels show that the detailed flow geometry toward the planet evolves over time, such that the distinct

$m = 2$  feature observed at all radii during early evolution is lost. At  $r = 0.5r_{\text{H}}$  we observe a superposition of  $m = 2$  and  $m = 1$  features, and at smaller radii  $m = 1$  dominates. This indicates that the inner CPD develops an elongated/elliptical structure, confirmed by examination of streamlines in the Hill sphere. The reason for this change in structure is not clear, but we conjecture that more pronounced gap opening at late times may modify the symmetry of the accretion flow onto the CPD arising from the inner and outer disk. This is an effect that can only arise in a global disk model and is not expected in local shearing box simulations. At late times the CPD midplane continues to display outflow away from the planet, and inflow remains confined to overlying latitudes above and below the midplane. Tanigawa et al. (2012) report that the midplane region continues to display outflow on scales as small as  $r = 0.03$ . Taking this result at face value suggests that further simulations are required that probe even deeper into the Hill sphere to examine at which radius the midplane region of the circumplanetary disk behaves as a classical accretion disk, instead of transporting mass away from the planet.

The situation described above changes only moderately when we consider the two non-isothermal runs, for which the geometry of the mass flux is shown in Figure 18. We note that the isothermal model N2 showed only modest temporal variation over short time intervals, so the plots in Figure 17 show averages taken over one orbital period. As discussed already, both of the non-isothermal models N1 and M1 showed higher levels of temporal variability, and Figure 18 displays averages taken over the last 50 orbits of the simulations.

When comparing the last four panels of Figure 17 with Figure 18 we see that the main features of the flow in and out of the Hill sphere at  $r = r_{\text{H}}$  are similar in all runs. The basic  $m = 1$  symmetry of the mass flux at smaller radii is also similar. The main differences arise because of the flattening of the CPD in model N2 which is not replicated in the hotter CPDs in runs N1 and M1.

Focusing first on the non-magnetized simulation N1, we note that inflow is observed at essentially all longitudes for high latitudes  $|\theta'| \gtrsim 30^\circ$ . This is true at all radii from  $r = 0.5r_{\text{H}}$  down to  $r = 0.1r_{\text{H}}$ , as seen in Figure 18. We remark that this is consistent with the flow field shown in Figure 7. Considering the flow at lower latitudes in the equatorial region, we see that for  $|\theta'| \lesssim 30^\circ$  there lies a contiguous band of inflow at all radii  $r \leq 0.5r_{\text{H}}$  that lies between  $\phi' \approx 330^\circ$  and  $\phi' \approx 90^\circ$ , straddling the substellar point. Moving round to longitudes lying between  $100 \lesssim \phi' \lesssim 330^\circ$  we see a well-defined band of outflow near the equator. These bands of inflow and outflow are also consistent with the flow field shown in Figure 7, which shows inflow through the hemisphere facing the star, and outflow near the midplane through the hemisphere facing away from the star. Summarizing, we can say that inflow occurs from high latitudes, causing gas to fall toward the planet onto a circumplanetary disk whose half opening angle is  $\simeq 30^\circ$ . The persistent bands of in- and outflow at all radii indicate that the flow within the CPD is decidedly non-circular, and instead exhibits an elongated or elliptical topology, similar to that observed in run N2 at late times.

Moving on to the magnetized run, we see that the mass flux geometry shown in the last four panels of Figure 18 are very similar to those described for run N1. Examination of individual snapshots during the run show significant time dependence on orbital time scales, but the average accretion flow in the magnetized disk looks similar to that in the viscous model.

We now consider the flow rate toward the planet as a func-



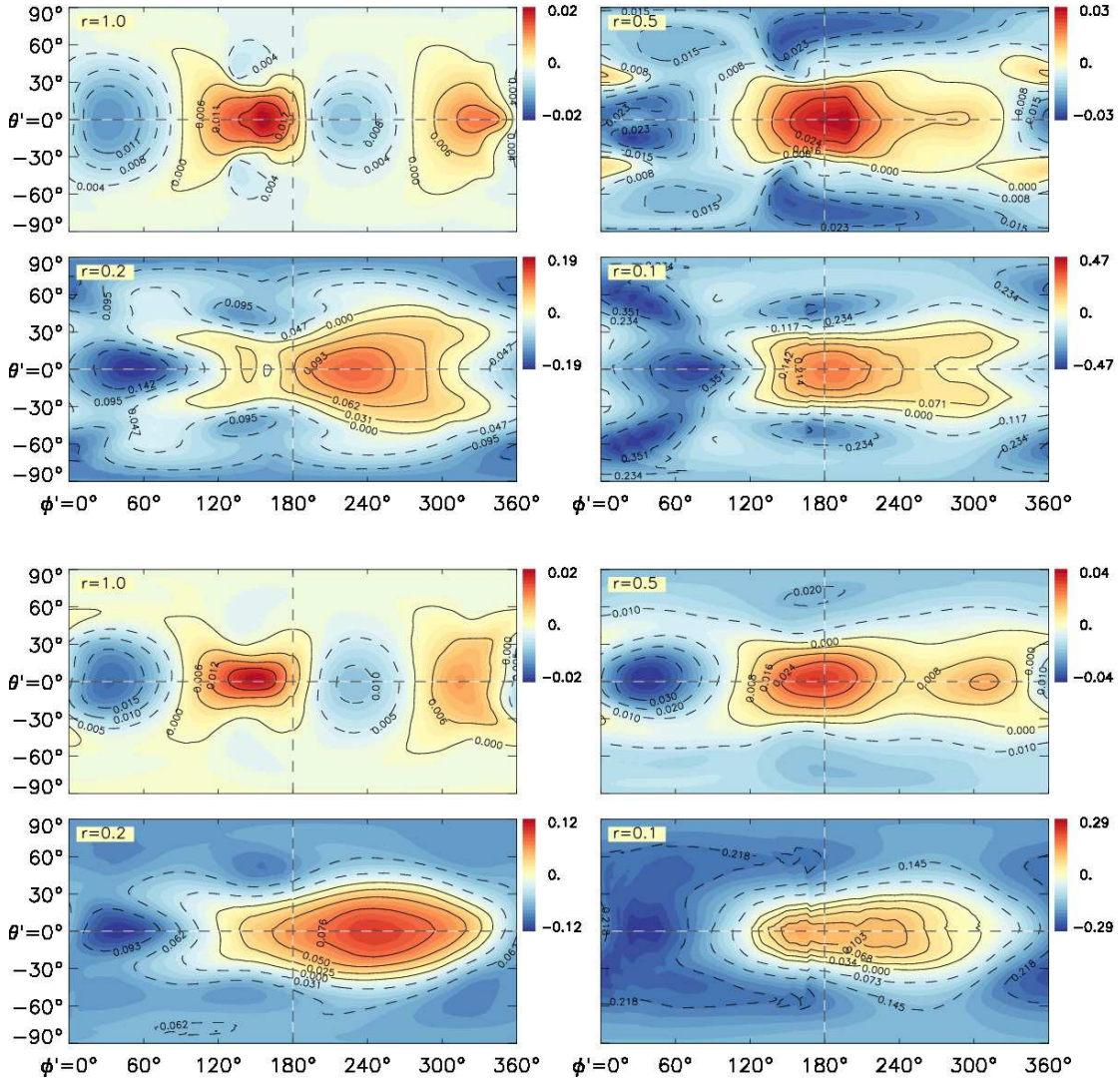


FIG. 18.— Same as Figure 17, but for the HD model, N1, (top four panels), and the MHD model (bottom four panels). Owing to the chaotic nature of the flow, time averages are taken over approximately 50 planet orbits to obtain a better picture of the long-term effective flow pattern.

tion of latitude only by azimuthally-averaging the mass fluxes displayed in Figures 17 and 18. These averaged mass fluxes are displayed in Figure 19. The top panel shows the isothermal model N2 at the end of the simulation, and this compares very well with previous results (cf. figure 6 in Tanigawa et al. 2012). In particular, we see that mass flow toward the planet at all radii occurs from high latitudes  $|\theta'| \geq 30^\circ$ , with the midplane region showing net outflow away from the planet at these radii. It is interesting to note that the inclusion of viscosity and angular momentum transport in the CPD in our run N2 leads to a net flow profile that agrees qualitatively with the inviscid model presented by Tanigawa et al. (2012). The non-isothermal HD case N1 is shown in the middle panel of Figure 19, and agrees reasonably well with the isothermal run at radii  $r = 1$  and  $0.5r_H$ , where outflow near midplane and inflow at high latitudes are observed. At  $r = 0.2r_H$  we see that the mass flux near the midplane is of small magnitude, and alternates between inflow and outflow. Net inflow at this radius is dominated by contributions from high latitudes. At  $r = 0.1r_H$  inflow occurs at all latitudes, with a modest contribution from the midplane region and a dominant contribution from higher latitudes. The results from model M1 shown in

the bottom panel are broadly consistent with model N1, and again display the important inflow contribution from high latitudes. We again note that the nature of the accretion flow is not dramatically altered by the inclusion of magnetic fields compared with the viscous disk model.

## 8. SUMMARY AND CONCLUSIONS

In this paper we have presented the results of global 3D hydrodynamic and magnetohydrodynamic simulations of accreting planets embedded in protoplanetary disks. The MHD simulation utilized a detailed ionization model from which Ohmic resistivity was calculated, leading to a disk with active surface layers that sustain MRI turbulence, and midplane regions that host a dead-zone where MRI turbulence is damped by resistivity. The hydrodynamic simulations adopted the  $\alpha$  model for anomalous viscosity, calibrated to give the same volume averaged stress as the magnetized disk, and were computed for the purpose of comparison with the turbulent disk simulation. One of the hydrodynamic simulations adopted a locally isothermal equation of state. The MHD run and the other hydrodynamic simulation both adopted an adiabatic equation of state combined with thermal relaxation, where the

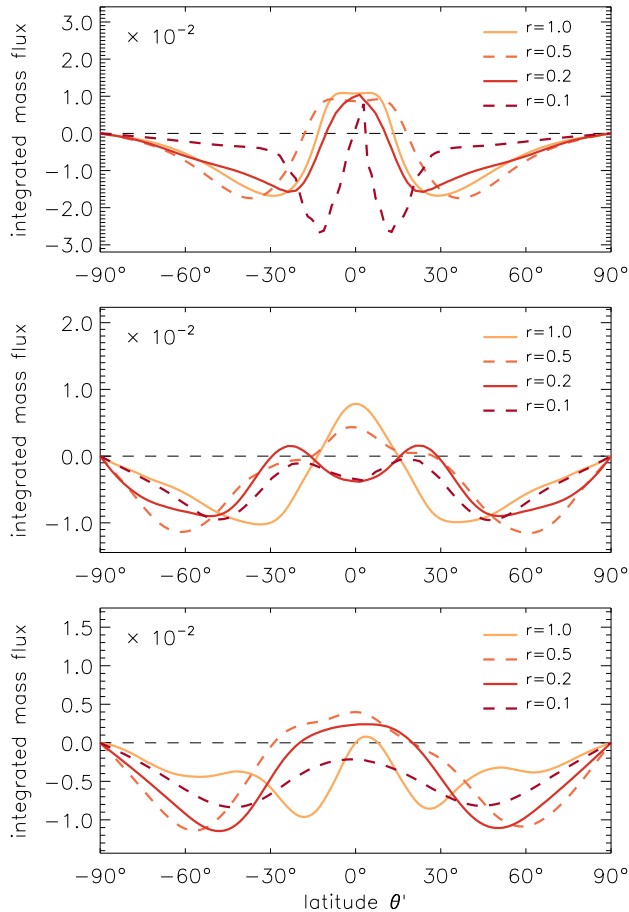


FIG. 19.— Azimuthally integrated mass fluxes (in code units) as a function of latitude for the isothermal HD model (top), the non-isothermal HD model (middle), and the non-isothermal MHD model (bottom). For low latitudes, and  $r \geq 0.5r_H$ , material is actually *expelled* (positive values).

temperature in the disk was continuously forced back toward its initial value on the local orbital time scale. All simulations used three levels of adaptive mesh refinement to resolve the region inside the planet Hill sphere. The accretion flow in these models is followed down to a radius equal to 5% of the Hill sphere. Interior to this a sink hole accretes inflowing gas, mimicking accretion onto the planet.

The main aims of this work are: (i) to examine gap formation in a layered protoplanetary disk and the influence of the changing ionization fraction of material near the planet as the gap opens, (ii) to examine the physical state and dynamical evolution of material that enters the planet Hill sphere, (iii) to measure the rate at which gas accretes onto a planet of mass  $100M_{\oplus}$ , placing it firmly in the regime of runaway gas accretion during giant planet formation. The main results may be summarized as follows:

- All simulations lead to gap formation in the vicinity of the planet. Accretion of gas into the Hill sphere leads to the formation of a rotationally supported circumplanetary disk. Significant accretion occurs onto the planet in all runs.
- The locally isothermal hydrodynamic simulation produces results very similar to those described previously by Machida et al. (2008) and Tanigawa et al. (2012). Infalling material leads to strong inflow toward the planet from *high latitudes*. Outflow away from the planet occurs in the mid-plane regions of the CPD for all radii down to  $0.1r_H$ , this

being the limit of where we can measure the flow geometry.

- Adoption of an adiabatic equation of state with thermal relaxation in a viscous hydrodynamic model leads to a warmer and thicker circumplanetary disk. Even in the presence of rapid cooling compressional heating increases the temperature to  $T \approx 2000$  K in the inner CPD. The increased pressure support reduces the accretion rate onto the planet during early evolution compared to the isothermal model. At late times, when higher angular momentum material accretes into the Hill sphere, the accretion rates converge.

- In agreement with the locally isothermal run, both the MHD and hydrodynamic simulations with thermal relaxation demonstrate that accretion toward the planet occurs from high latitudes. The midplane region of the CPD displays net outflow away from the planet down to radii  $r \geq 0.2r_H$ .

- Gap opening in the MHD simulation leads to ignition of the dead-zone into a turbulent state as X-rays and cosmic rays penetrate the gap region. The global structure of the disk is one in which accretion occurs in the active surface layers far from the planet, with the midplane region there being largely inert. Near the planet there is deep gap where the ionization fraction allows development of MRI-turbulence.

- Enlivening the gap in the MHD simulation causes the accreting planet to be embedded in a turbulent environment. Accretion onto the planet becomes stochastic, and the flow in the Hill sphere displays significant temporal variability. The CPD has a surface density  $\sim 30 \text{ g cm}^{-2}$  between its outer edge at  $\sim 0.5$  Hill radii and the inner boundary at 5% of the Hill radius. This is low enough to be sufficiently ionized by X-rays and cosmic rays to sustain the MRI. Our measurement of the Elsasser number there suggests that the circumplanetary disk should indeed be MRI active, at least in its outer regions.

- Gas accretion into the gap and planet Hill sphere occurs largely from the active surface layers of the surrounding protoplanetary disk. As gas enters the gap it is pulled toward the midplane by the star and planet gravity, dragging the (largely azimuthal) magnetic field with it. Gas and magnetic field lines that enter the Hill sphere join the rotating circumplanetary disk, leading to the generation of helical magnetic fields. These launch what appear to be sporadic magneto-centrifugally driven outflows. These are generally found to be loosely collimated, but we have observed at least one extended time interval during which a highly collimated jet was launched from the CPD region. The protoplanetary jet does not influence strongly the gas accretion rate onto the planet.

- Stochastic accretion into the Hill sphere causes the direction of the angular momentum vector of material there to vary significantly. Our model suggests that CPDs display substantial time variability in their tilt angle, amounting to changes  $\sim 10^\circ$  on orbital time scales. Although we cannot model the inner regions of the CPD explicitly, we speculate that oscillations in global tilt angle will allow propagation of bending waves into the inner satellite forming region, creating a source of disturbance that may influence the formation of regular satellite systems. In this scenario, it seems likely that satellite building blocks orbiting within the inner CPD will develop mutually inclined orbits if they are strongly coupled to the gaseous CPD, leading to slower growth of the satellites.

- The accretion rate onto the planet in the MHD simulation reaches a steady value of  $\dot{M} = 8 \times 10^{-3} M_{\oplus} \text{ yr}^{-1}$ , large

enough for a Saturn-mass planet to become a Jovian planet in  $\sim 3 \times 10^4$  yr, much shorter than the expected disk life-time. This steady state is reached  $\sim 100$  orbits after insertion of the planet. The accretion rates in the viscous, hydrodynamic simulations continue to fall below this value, and do not reach steady values by the end of the runs. This is a consequence of the accretion flow in the magnetized disk being confined to the active layers where the magnetic stresses are large. This flow is impervious to tidal truncation and gap formation by the planet, even if its mass becomes quite large, because the effective viscous stress there is large (i.e.  $\alpha \gtrsim 0.1$ ), leading to saturation of the mass accretion rate at a higher value than obtained in a viscous model with a constant  $\alpha$  value.

### 8.1. Implications

The above results have a number of implications for planet and satellite formation. The feeding of gas into the gap region from the surface layers of the PPD may have important consequences for the chemistry and dust content of the gas that eventually accretes onto the planet, as dust settling and sequestration in the dead-zone may reduce the heavy element content of this gas as it accretes through the disk. One implication is that gas accreted through a gap in a disk with active surface layers and a midplane dead-zone will have lower opacity. Models of giant planet formation (e.g. Pollack et al. 1996; Papaloizou & Nelson 2005; Movshovitz et al. 2010) show that the upper-envelope opacity is crucial in determining the envelope accretion time scale. A low mass planet (i.e.  $5\text{--}10M_{\oplus}$ ) deeply embedded in a disk without a gap will probably not experience a significant reduction in opacity of the accreted gas as it originates from the local midplane during the early phases of envelope accretion. If placed in a region of the disk where the scale-height is much smaller, however, such as in the inner few tenths of an au where  $h \lesssim 0.02$  (depending on the viscous dissipation rate, see e.g. D’Angelo & Marzari 2012) gap formation is expected even for planets with masses  $< 10M_{\oplus}$  and these may then accrete metal-poor, low opacity gas, reducing the core mass required to build-up a substantial gaseous envelope. This may provide an explanation for the low mass and low density planets that have been discovered by the Kepler mission such as “Kepler 11e” (Lissauer et al. 2011). One potential caveat is that most protoplanetary disk models have a transition where the dead-zone disappears and the disk becomes fully active at a distance of a few tenths of an au from the central star (Gammie 1996; Ilgner & Nelson 2006). We note that a planetary core accreting gas from this disk region will still accrete metal-poor gas, because gas arriving at the inner regions will have accreted through the disk surface layers from further out in the disk where dust settling will have reduced the heavy element content of this gas. Examination of this idea will require development of detailed planetary envelope accretion models in which the usual outer boundary condition that matches the envelope onto the background protoplanetary nebula model will need to be replaced with one that assumes the envelope has a quasi-free surface, perhaps surrounded by a thick circumplanetary disk. Such calculation were presented by Papaloizou & Nelson (2005) for giant planets undergoing runaway gas accretion, but have not been performed for planets in the earlier phase of quasi-static gas settling. Alternatively this scenario could be explored using 3D radiation-hydrodynamic simulations similar to those presented by Ayliffe & Bate (2009a,b).

The comments above concerning the heavy element content of accreted gas also have implications for the formation

of satellite systems. Tanigawa et al. (2012) have noted already that delivery of gas deep into the Hill sphere from high latitudes may lead to accretion of low-metallicity gas onto the inner CPD if grain growth and settling have occurred in the surrounding PPD. The fact that low-metallicity gas is delivered into the gap largely from the active surface layers simply reinforces this point.

The temperatures that we obtained for the inner CPDs in the models with applied cooling should not be taken too seriously given our crude thermal model. In spite of this, it is noteworthy that inner temperatures obtained  $T \simeq 2000$  K are similar to those reported by Klahr & Kley (2006) in their radiation-hydrodynamic simulations. Temperatures in excess of  $T \simeq 1500$  K are large enough to vaporise refractory materials in addition to volatiles such as water ice, so taken at face value our results and those of Klahr & Kley (2006) indicate that satellite building material is unlikely to be transported to the vicinity of the planet by this early-stage accretion flow. Achieving temperatures low enough to support condensation of ices for building icy satellites clearly requires a phase of evolution in which material is delivered to the inner regions of CPDs at much lower rates because of the dependence of the temperature on the local gas accretion rate.

### 8.2. Concluding remarks

Although the model we have presented of a planet accreting gas from a layered protoplanetary disk represents a significant step forward in terms of complexity, realism and numerical resolution, there are numerous omissions to the physical model that need to be addressed in future work before we can be confident that gas accretion rates onto forming giant planets are fully understood. The non-ideal MHD model that we have adopted neglects the potentially important effects of ambipolar diffusion and Hall EMFs, both of which may significantly modify the results we have presented (Wardle & Salmeron 2012; Bai & Stone 2013). In a future paper we will be particularly interested in examining the influence of ambipolar diffusion in the gap region. The low densities there may allow this effect to quench the turbulent nature of the flow in the gap, and this will have significant consequences for the time dependence of the flow in the Hill sphere.

A related issue that needs to be explored is the transport of stellar X-rays into the gap region, as this is crucial for determining the ionisation levels close to the giant planet. In this work we have taken a simple approach and adopted results from the model of Igea & Glassgold (1999) in which X-rays are scattered vertically toward the disk midplane from the overlying disk atmosphere, with attenuation depending simply on the column density. This model, however, does not account for the effects of gap opening and a more accurate approach will require transfer calculations of X-rays being scattered into the gap. A further refinement would be to include the effects of X-ray flares. These lead to both substantial increases in the X-ray flux, and also to a substantial hardening of the spectra (Arzner et al. 2007; Franciosini et al. 2007; Getman et al. 2008). Given that hard X-rays are able to penetrate more deeply into the disk this may influence the ionization of material in the vicinity of the planet.

A proper treatment of the gas thermodynamics is also needed. This is illustrated by the fact that during the time before a steady state has been achieved, our locally isothermal model displays a higher gas accretion rate than in the models with an adiabatic equation of state and local cooling. In

other words, thermodynamics play a role in regulating the accretion rate prior to gap formation while the planet is deeply embedded in the PPD. Our simulations suggest that if giant planets form in protoplanetary disks with properties similar to minimum mass solar nebula models (Hayashi 1981), then these disks are very capable of supplying large amounts of gas to forming planets that can allow them to grow to super-Jovian masses. The fact that massive planets are relatively rare suggests either that the available gas reservoir during gas accretion is smaller than in a minimum mass disk, or that accretion into the Hill sphere and onto the planet experiences a bottle-neck. Our simulations suggest that compressive heating and inefficient cooling in the Hill sphere can contribute to slowing the accretion, although the radiation-hydrodynamic simulations of Ayliffe & Bate (2009b) indicate that rapid runaway gas accretion still occurs when radiative processes are accounted for. Inefficient angular momentum and mass transport through the inner regions of the circumplanetary disk, on scales smaller than we have been able to model may also play a role here, as considered for example in the disk models of Martin & Lubow (2013).

The possibility, however, that mass can build-up in the inner circumplanetary disk to levels that allow gravitational instabilities to develop, which then transport angular momentum

efficiently, may signify that any model that allows efficient supply of mass into the Hill sphere must also lead inevitably to substantial accretion onto the planet. If MRI turbulence does not transport mass and angular momentum efficiently, then gravitational instabilities may develop to do the job instead, leading to the same net result of an efficiently accreting circumplanetary disk. This favors a picture of giant planet formation in which the final mass is determined by the flow of gas from circumstellar to circumplanetary disk, rather than peculiarities associated with the flow within the planet's Hill sphere. Demonstration of this basic idea, however, will require substantial further work.

We thank the anonymous referee for useful comments that led to an improvement of this paper. Part of the research was carried out at the Jet Propulsion Laboratory, California Institute of Technology, under a contract with the National Aeronautics and Space Administration. The simulations presented in this paper were run on the QMUL HPC facility. Three-dimensional imagery produced by VAPOR (Clyne et al. 2007, [www.vapor.ucar.edu](http://www.vapor.ucar.edu)), a product of the Computational Information Systems Laboratory at the National Center for Atmospheric Research.

## REFERENCES

- Alexiades, V., Amiez, G., & Gremaud, P.-A. 1996, *Communications in Numerical Methods in Engineering*, 12, 31
- Arzner, K., Güdel, M., Briggs, K., Telleschi, A., & Audard, M. 2007, *A&A*, 468, 477
- Ayliffe, B. A., & Bate, M. R. 2009a, *MNRAS*, 397, 657
- 2009b, *MNRAS*, 393, 49
- Bai, X.-N., & Stone, J. M. 2013, *ApJ*, 769, 76
- Balbus, S. A., & Hawley, J. F. 1998, *RvMP*, 70, 1
- Balsara, D. S., & Meyer, C. 2010, (*astro-ph:1003.0018*)
- Balsara, D. S., & Spicer, D. S. 1999, *JCoPh*, 149, 270
- Boss, A. P. 1998, *ApJ*, 503, 923
- Bryden, G., Chen, X., Lin, D. N. C., Nelson, R. P., & Papaloizou, J. C. B. 1999, *ApJ*, 514, 344
- Canup, R. M., & Ward, W. R. 2002, *AJ*, 124, 3404
- 2006, *Nature*, 441, 834
- Clyne, J., Mininni, P., Norton, A., & Rast, M. 2007, *New Journal of Physics*, 9, 301
- D'Angelo, G., Henning, T., & Kley, W. 2003, *ApJ*, 599, 548
- D'Angelo, G., & Marzari, F. 2012, *ApJ*, 757, 50
- de Val-Borro, M., Edgar, R. G., Artymowicz, P., et al. 2006, *MNRAS*, 370, 529
- Fendt, C. 2003, *A&A*, 411, 623
- Flock, M., Dzyurkevich, N., Klahr, H., & Mignone, A. 2010, *A&A*, 516, A26+
- Franciosini, E., Pillitteri, I., Stelzer, B., et al. 2007, *A&A*, 468, 485
- Fromang, S., & Nelson, R. P. 2006, *A&A*, 457, 343
- Gammie, C. F. 1996, *ApJ*, 457, 355
- Gardiner, T. A., & Stone, J. M. 2008, *JCoPh*, 227, 4123
- Getman, K. V., Feigelson, E. D., Micela, G., et al. 2008, *ApJ*, 688, 437
- Goodman, J., & Rafikov, R. R. 2001, *ApJ*, 552, 793
- Gressel, O., Nelson, R. P., & Turner, N. J. 2011, *MNRAS*, 415, 3291
- 2012, *MNRAS*, 422, 1140
- Hawley, J. F., Richers, S. A., Guan, X., & Krolik, J. H. 2013, *ApJ*, 772, 102
- Hayashi, C. 1981, *Progress of Th. Phys. Suppl.*, 70, 35
- Igea, J., & Glassgold, A. E. 1999, *ApJ*, 518, 848
- Ilgner, M., & Nelson, R. P. 2006, *A&A*, 445, 205
- Klahr, H., & Kley, W. 2006, *A&A*, 445, 747
- Kley, W. 1999, *MNRAS*, 303, 696
- Larwood, J. D., Nelson, R. P., Papaloizou, J. C. B., & Terquem, C. 1996, *MNRAS*, 282, 597
- Lin, D. N. C., & Papaloizou, J. 1986, *ApJ*, 309, 846
- Lin, D. N. C., & Papaloizou, J. C. B. 1993, in *Protostars and Planets III*, ed. E. H. Levy & J. I. Lunine, 749–835
- Lissauer, J. J., Fabrycky, D. C., Ford, E. B., et al. 2011, *Nature*, 470, 53
- Londrillo, P., & del Zanna, L. 2004, *JCP*, 195, 17
- Lubow, S. H., Seibert, M., & Artymowicz, P. 1999, *ApJ*, 526, 1001
- Machida, M. N., Inutsuka, S.-i., & Matsumoto, T. 2006, *ApJ*, 649, L129
- Machida, M. N., Kokubo, E., Inutsuka, S.-i., & Matsumoto, T. 2008, *ApJ*, 685, 1220
- Machida, M. N., Kokubo, E., Inutsuka, S.-i., & Matsumoto, T. 2010, *MNRAS*, 405, 1227
- Martin, R. G., & Lubow, S. H. 2011, *MNRAS*, 413, 1447
- 2013, *MNRAS*
- Meyer, C. D., Balsara, D. S., & Aslam, T. D. 2012, *MNRAS*, 422, 2102
- Miyoshi, T., & Kusano, K. 2005, *JCoPh*, 208, 315
- Mizuno, H. 1980, *Progress of Theoretical Physics*, 64, 544
- Mosqueira, I., & Estrada, P. R. 2003, *Icarus*, 163, 198
- Movshovitz, N., Bodenheimer, P., Podolak, M., & Lissauer, J. J. 2010, *Icarus*, 209, 616
- Muto, T., Suzuki, T. K., & Inutsuka, S.-i. 2010, *ApJ*, 724, 448
- Nelson, R. P., Gressel, O., & Umurhan, O. M. 2012, *astro-ph:1209.2753*
- Nelson, R. P., & Papaloizou, J. C. B. 2003, *MNRAS*, 339, 993
- Nelson, R. P., Papaloizou, J. C. B., Masset, F., & Kley, W. 2000, *MNRAS*, 318, 18
- Oishi, J. S., & Mac Low, M.-M. 2011, *ApJ*, 740, 18
- Okuzumi, S., & Hirose, S. 2011, *ApJ*, 742, 65
- Paardekooper, S.-J., & Mellema, G. 2008, *A&A*, 478, 245
- Papaloizou, J. C. B., & Lin, D. N. C. 1995, *ARA&A*, 33, 505
- Papaloizou, J. C. B., & Nelson, R. P. 2005, *A&A*, 433, 247
- Papaloizou, J. C. B., Nelson, R. P., & Snellgrove, M. D. 2004, *MNRAS*, 350, 829
- Pierens, A., & Nelson, R. P. 2010, *A&A*, 520, A14
- Pinte, C., Padgett, D. L., Ménard, F., et al. 2008, *A&A*, 489, 633
- Pollack, J. B., Hubickyj, O., Bodenheimer, P., et al. 1996, *Icarus*, 124, 62
- Quillen, A. C., & Trilling, D. E. 1998, *ApJ*, 508, 707
- Sano, T., Miyama, S. M., Umebayashi, T., & Nakano, T. 2000, *ApJ*, 543, 486
- Saumon, D., & Guillot, T. 2004, *ApJ*, 609, 1170
- Shabram, M., & Boley, A. C. 2013, *ApJ*, 767, 63
- Skinner, M. A., & Ostriker, E. C. 2010, *ApJS*, 188, 290
- Tanigawa, T., Ohtsuki, K., & Machida, M. N. 2012, *ApJ*, 747, 47
- Turner, N. J., Choukroun, M., Castillo-Rogez, J., & Bryden, G. 2012, *ApJ*, 748, 92
- Turner, N. J., & Drake, J. F. 2009, *ApJ*, 703, 2152
- Turner, N. J., Lee, M. H., & Sano, T. 2013, *arXiv astro-ph:1306.2276*
- Umebayashi, T., & Nakano, T. 1981, *PASJ*, 33, 617
- 2009, *ApJ*, 690, 69
- Uribe, A. L., Klahr, H., Flock, M., & Henning, T. 2011, *ApJ*, 736, 85
- Ward, W. R. 1997, *Icarus*, 126, 261
- Wardle, M. 2007, *Ap&SS*, 311, 35
- Wardle, M., & Salmeron, R. 2012, *MNRAS*, 422, 2737

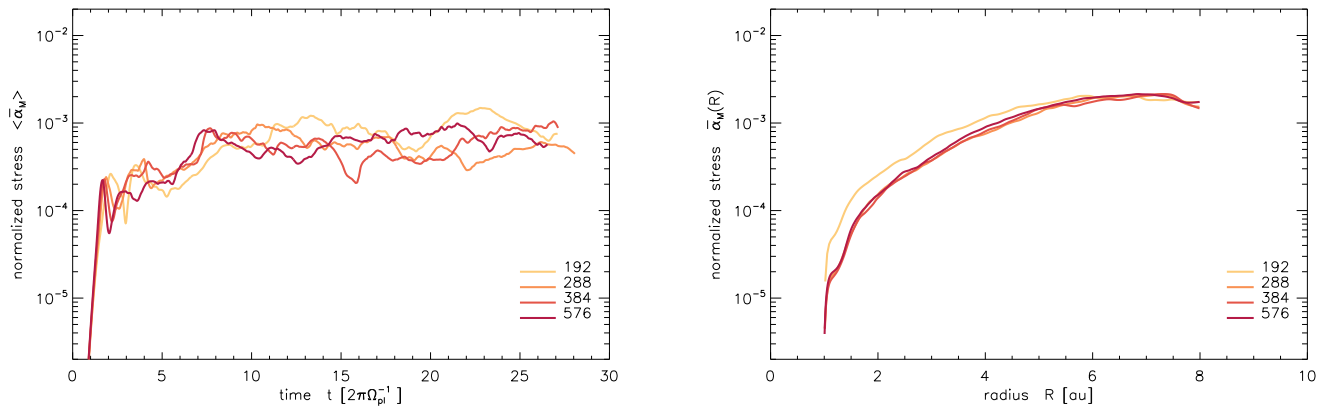


FIG. 20.— Resolution study of the unperturbed disk model in the absence of mesh refinement. Numbers are for the adopted number of radial grid cells; the resolution in the vertical and azimuthal directions are scaled accordingly. *Left*: Time series of the volume averaged Maxwell stress evaluated in the radial range  $3 \leq r \leq 4$  au. *Right*: Radial profile of the volume- and time-averaged Maxwell stress.

Watson, A. M., Stapelfeldt, K. R., Wood, K., & Ménard, F. 2007, *Protostars and Planets V*, 523  
Winters, W. F., Balbus, S. A., & Hawley, J. F. 2003, *ApJ*, 589, 543

Ziegler, U. 2004, *JCoPh*, 196, 393  
— 2011, *JCoPh*, 230, 1035  
Zingale, M., Dursi, L. J., ZuHone, J., et al. 2002, *ApJS*, 143, 539

#### APPENDIX

It is clear that insufficient numerical resolution will lead to erroneous results being obtained in terms of stresses and accretion rates. For example, Fromang & Nelson (2006) presented one of the first systematic studies of MRI-driven turbulence in vertically stratified global disk models and found that approximately 6 cells were required to resolve the fastest growing MRI modes in order for nonlinear MRI-turbulence to be sustained in disks containing weak net-toroidal magnetic fields. In recent work the influence of numerical resolution in producing robust results has been emphasized strongly (Hawley et al. 2013), where it has been suggested that between 20-30 cells per unstable MRI wavelength are required to obtain reliable results in disk models that sustain MRI turbulence throughout (i.e. no dead zone present).

The basic disk model, M1, presented in the main body of this paper has a significantly lower resolution than this, and so we have computed a suite of test calculations to examine the influence of changing the numerical resolution in the simulations. These calculations did not use mesh refinement. The size of the azimuthal domain used was  $\pi/4$  instead of  $\pi/2$ , but adopting the same grid size ratio  $\Delta_r : \Delta_\phi$  as in the original simulation. The time evolution of the Maxwell stress (as defined in Equation (13) of Fromang & Nelson 2006) evaluated between the radii  $3 \leq r \leq 4$  au for the different models is shown in the left-hand panel of Figure 20. The number shown in the inset is the number of radial grid cells,  $N_r$ , where  $N_r = 384$  in model M1. When changing the radial resolution we also changed the resolution in the other dimensions by the same factor. We see that there is little evidence of a systematic trend in the results as a function of numerical resolution. This point is further supported by the right-hand panel of the same figure, where we show radial profiles of the temporally-averaged Maxwell stresses. Apart from the low-resolution model with 192 grid cells in radius, all models produce nearly indistinguishable results.

The reasons for this are two-fold. First, we adopt a net-vertical magnetic field in our simulations that is essentially conserved throughout the runs. This has the effect of reducing the influence of the numerical resolution on the results because we do not rely on any sort of disk dynamo to maintain the large-scale vertical field. Second, the presence of the dead zone means that only a relatively narrow region of the disk above the midplane is susceptible to growth of the MRI – there the fields are generally quite strong (compared to the gas pressure), leading to MRI developing on comparatively larger scales. By contrast, the resolution requirements are more severe in a disk where turbulence can also develop near the midplane because the value of  $\beta_P \equiv P_{\text{gas}}/P_{\text{mag}}$  will be larger there. The low density and pressure in the upper disk layers means that  $\beta_P$  is fairly small (between 20–30), and this allows the MRI to be quite well resolved even for weak fields. For ideal MHD, the wavelength of the fastest growing mode can be approximated by  $\lambda_{\text{MRI}} \equiv 2\pi v_A/\Omega$ . Using the relation  $c_s = H\Omega$ , and noting that  $\beta_P = c_s^2/v_A^2$ , we can express this as  $\lambda_{\text{MRI}} = 2\pi H/\sqrt{\beta_P}$ . With this relation, we estimate that in our case  $\lambda_{\text{MRI}}$  is on the order of the pressure scale height itself and thus adequately resolved.

Another issue of potential importance is the role of mesh refinement in determining the evolution of the MRI in the disk and the strength of the turbulent stresses. In a disk without a dead zone, where MRI turbulence can develop throughout the body of the disk, we would expect the region in which mesh-refinement is applied to show enhanced activity compared to the surrounding disk regions. This is because shorter wavelength MRI modes will be resolved in this region, potentially boosting the strength of the turbulence there. In our model, however, the mesh refinement is applied in a spherical region centered around the planet near the midplane. The refined region therefore lies almost entirely within the dead zone and has essentially no effect on the turbulence in the active zones near the disk surfaces. We have tested this by running a simulation with refinement applied around the nominal planet location, but with the planet’s gravity switched off. When the planet gravity is switched on, however, gap formation ensues and we might be concerned that developing turbulence in the annular region centered on the planet semi-major

axis will be affected by the refinement. We note, however, that the refinement is applied in a spherical region around the planet, and therefore does not extend far in azimuth. As such, we conclude that the refinement has little influence on the turbulence in the surrounding protoplanetary disk, and is only effective in the region where the planet gravity dominates, allowing small scale fluid and magnetic structures to be resolved there, as intended.